Fabrication of Lithium-Ion Pouch Cells with Reversible Shutdown Membrane Separator

Matthew Newman

Spring 2020

An Undergraduate Honors Thesis

Presented in Partial Fulfillment of Graduation with Honors Research Distinction in the Department of Mechanical Engineering of The Ohio State University

Oral Defense Committee:

Dr. Vishnu Sundaresan (Advisor)

Dr. Hanna Cho

Abstract

Batteries that power electrical vehicles, especially the safety concerns and performance limitations, are of significant interest as the thrust for sustainable transportation continues. Li-ion batteries are prevalent in these vehicles and many consumer electronics due to their advantages over other battery chemistries. Thermal runaway is a major safety concern of batteries that can result in fires or explosions, and li-ion architectures are at a higher risk. Limited charge and discharge rates contribute to electric vehicles' inability to fully compete with internal combustion engine vehicles. The objective of this research is to transition the use of a reversible shutdown membrane separator (RSMS) in a Swagelok cell to a pouch cell, an architecture used in commercial applications, and find a cost-effective alternative to gold in RSMS fabrication. Through a redox event, a RSMS can operate as an ion source or sink, which can internally and reversibly prevent thermal runaway or provide a power boost.

A novel fabrication method was developed for a three-electrode li-ion pouch cell with a RSMS as a third active electrode. The RSMS shape was tailored for a built-in current lead and melt tape parameters were optimized for effective sealing between the lead and pouch. Once fabricated, charge-discharge cycling and real time testing of the pouch cell with a RSMS was performed to examine the cell charge-discharge cycling capacities and validate the RSMS worked reversibly for preventing thermal runaway or providing a power boost. Alternatives to gold, most of which are common in li-ion batteries (aluminum, nickel, aluminum/titanium, and nickel/titanium), were explored in the fabrication of the RSMS. Cyclic voltammetry was used to examine the electrochemical function and cyclabilities compared to gold.

The charge-discharge cycling capacities of the cell with a RSMS were comparable to baseline cells for a reduced state membrane and lower for an oxidized state membrane. Real time results showed the RSMS could remove anode current for ~30-60 seconds to prevent thermal runaway or provide a power boost for ~60 seconds without changing the constraints of the power source or load. Nickel was determined to be a feasible candidate to replace gold due to fabrication ease and a reasonable filling efficiency of 31.9% compared to gold's 42.5%. This is the first technique (to our knowledge) for fabricating three electrode pouch cells with a third active electrode. This fabrication technique for three active electrode pouch cells could be used for different third active electrodes to expand the capabilities of battery cells. The use of an active membrane separator could be extended to implement other types of active membrane separators instead of standard passive separators. Li-ion pouch cells or other battery architectures with a RSMS will provide enhanced safety with thermal runaway protection and improved performance capability with power boost functionality.

Acknowledgements

I would like to thank my advisor Dr. Vishnu Sundaresan for introducing me to the project and his technical oversight throughout the project. He provided me with a clear explanation of the project at the beginning and made sure the significance of the research was understood. I am also grateful for the guidance he has given me related to graduate school.

I would also like to thank Dr. Travis Hery for bringing me up to speed at the start of the project, the numerous questions of mine he has answered, and the knowledge and resources he has provided me for a better understanding of the electrochemical concepts for the research. He would always help troubleshoot or provide guidance when needed and his help has been invaluable over the course of the project.

I would like to acknowledge Ford for their financial support and technical guidance during the project through the Ford-OSU Alliance.

Table of Contents

List of Figures

List of Tables

Chapter 1: Introduction

1.1: Lithium-ion Batteries and the Limitations

With the ever-growing concerns of climate change, emissions, and sustainability, batteries continue to become more prevalent. Lithium-ion batteries are often the battery chemistry of choice due to high energy and power density [1]. An overview of lithium-ion battery operation is shown in Figure 1.

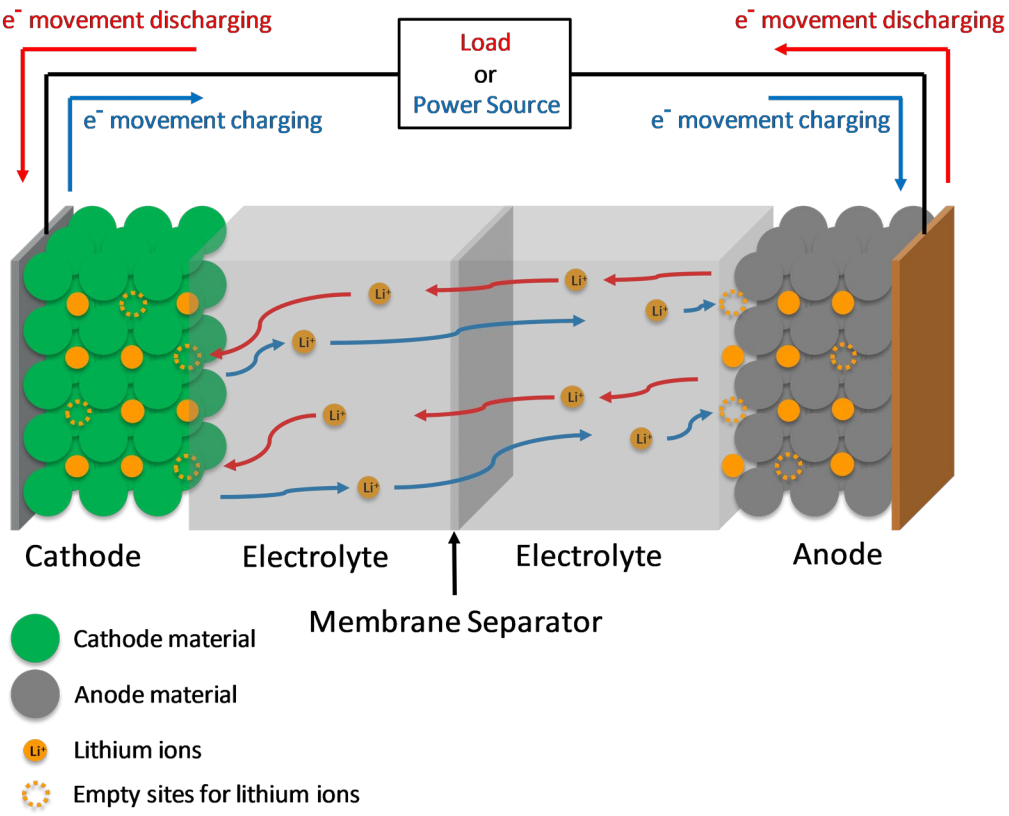

Figure 1: Standard two electrode lithium-ion battery operation.

Some standard battery packaging types are shown in Figure 2. Cylindrical cells are the most standardized of the different packages, and both cylindrical and prismatic cells include significant amounts of structural material in them. Pouch cells have very little structural material

which results in a nearly maximized packaging density (ratio of active to inactive materials) [2]. Due to the nearly maximized packaging density, there is significant interest in pouch cells.

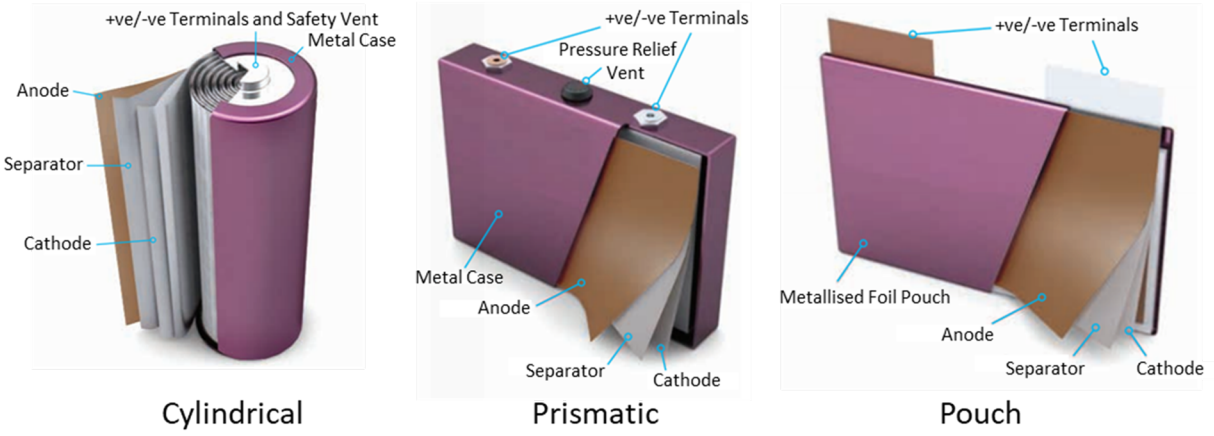

Figure 2: Structure of different battery packaging types.
[Source: Johnson Matthey Battery Systems]

However, there are still concerns and limitations of lithium-ion chemistries. Thermal runaway is a major safety concern with the potential to cause battery fires or explosions [3]. Thermal runaway is caused by a chain reaction initiated with a temperature rise in the cell, typically resulting from an internal short [4]. As the cell temperature increases, side reactions begin such as the decomposition of the solid electrolyte interface (SEI) at the anode. These side reactions release more heat, further increasing the temperature which in turn increases the rate of the side reactions. This loop results in the temperature of the cell to continue to increase leading to a fire or explosion. The resulting catastrophe from thermal runaway in lithium-ion batteries will often be in widespread news such as the Samsung Note 7 batteries exploding or Tesla vehicles catching on fire.

Another limitation of lithium-ion batteries is the C-rates for charging and discharging. C-rates are normalized charging/discharging rates for the battery capacity such that a 1C rate corresponds to a one-hour charge/discharge, 1/2C corresponds to a two-hour charge/discharge and so on. Increasing the C-rate by merely increasing current leads to more losses from the greater heat generation and increases the risk for thermal runaway. The increase in C-rate also results in a sharp decline in battery capacity [5]. This is a fundamental limitation for many types of electrochemical energy systems as shown in Figure 3. This limitation is a major factor in commercial electric vehicles compromising on driving range versus recharge time compared to internal combustion engine vehicles. Delayed mass market adoption of electric vehicles could in part be due to this compromise, where an internal combustion engine vehicle only takes a few minutes to fuel up for hundreds of miles of range, an electric vehicle will take a few hours to charge. The miles per minute (MPM) for electric versus internal combustion engine vehicles is shown in Figure 4. This metric is how many miles of range a vehicle has per minute of recharging/refueling time.

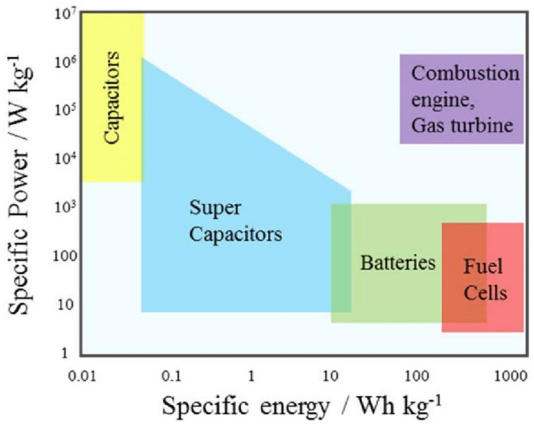

Figure 3: Ragone plot comparing the specific power and specific energy of electrochemical energy systems to traditional combustion energy systems [6].

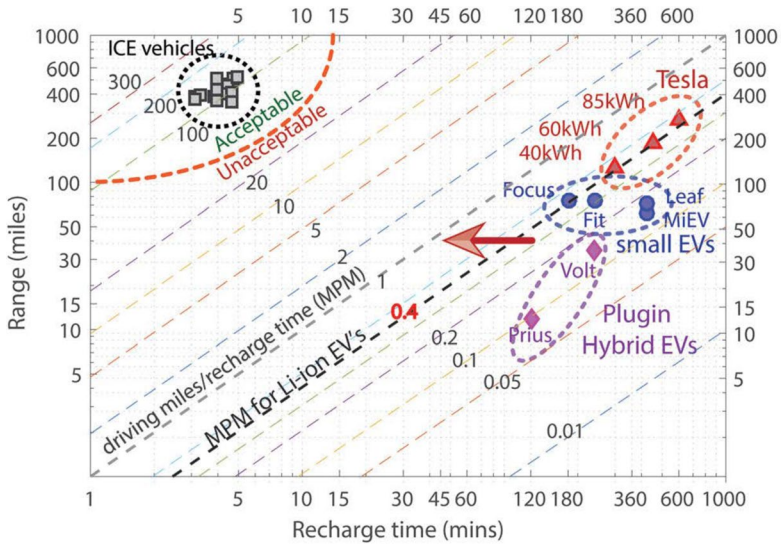

Figure 4: Plot of electric vehicles range (miles) versus recharge time (min) giving a metric of miles per min (MPM) for comparison against internal combustion engine vehicles [7].

1.2: Current Methods to Counteract Thermal Runaway

A few methods currently exist for counteracting thermal runaway in lithium-ion batteries, however, these methods either do not internally prevent the flow of ions or are irreversible. A thermoresponsive polymer switching material (TRPS), shown in Figure 5, becomes nonconductive at a transition temperature corresponding to near thermal runaway conditions and returns to normal conductivity at room temperature [8]. This does not prevent the flow of ions and as a result requires accurate prediction of the temperature before thermal runaway would begin. Two methods that do prevent the flow of ions are thermally activated additives or shutdown separators. Both methods are irreversible, permanently disabling the battery. Thermally activated additives, shown in Figure 6, sit on top of the electrode material and at the transition temperature melt to coat the electrodes rendering them non-conductive [9]. The shutdown separator, shown in Figure 7, starts to melt at the transition temperature to cover up the pores [10].

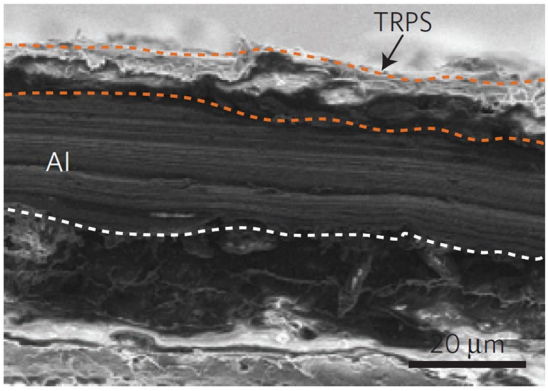

Figure 5: Thermoresponsive polymer switching material (TRPS) on Al current collector [8].

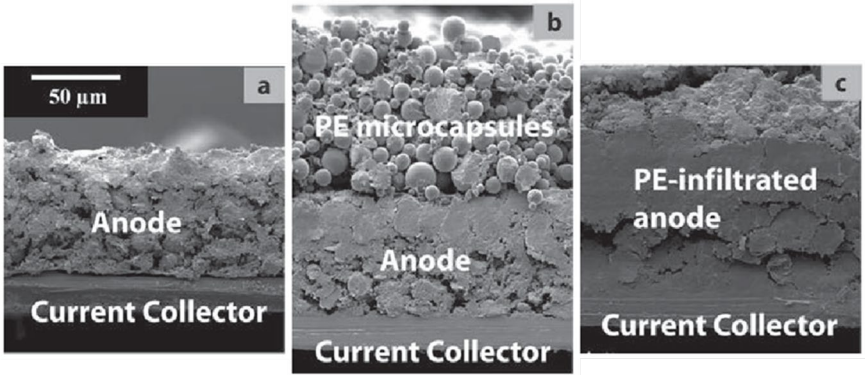

Figure 6: Thermally activated additive (PE microcapsules) [9].

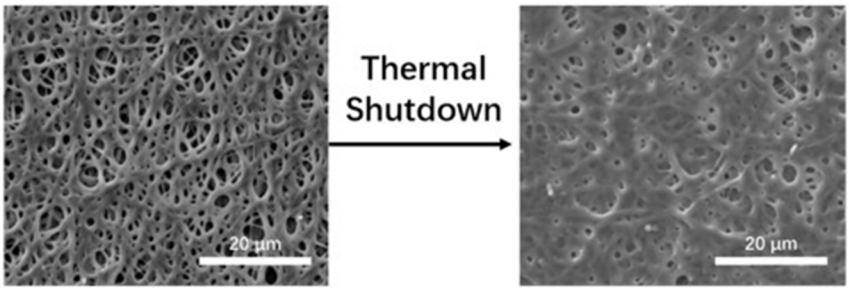

Figure 7: Shutdown separator [10].

1.3: Reversible Shutdown Membrane Separator

A reversible shutdown membrane separator (RSMS) [11], which is an ionic redox transistor [7] applied as the membrane separator in a battery, can internally and reversibly counteract thermal runaway by preventing ion flow between electrodes. The RSMS can also provide periods of high-power charge or discharge, increasing the effective C-rate without sacrificing the capacity of the battery. Applications of this capability include rapid charging or discharging of the battery. An outline of the construction and operation of an ionic redox transistor as a RSMS is shown in Figure 8. PPy(DBS) is a conducting polymer that is redox active, which enables the functionality of the RSMS. Based on the potential or current applied across the RSMS, it will undergo a reduction or oxidation event. During reduction there is cation ingress so the RSMS acts as an ion sink. In the operation of a lithium-ion battery, the RSMS will deplete Li^+ ions at whichever electrode it is reduced against. During oxidation there is cation egress so the RSMS acts as an ion source. The RSMS will provide excess Li^+ ions to whichever electrode it is oxidized against.

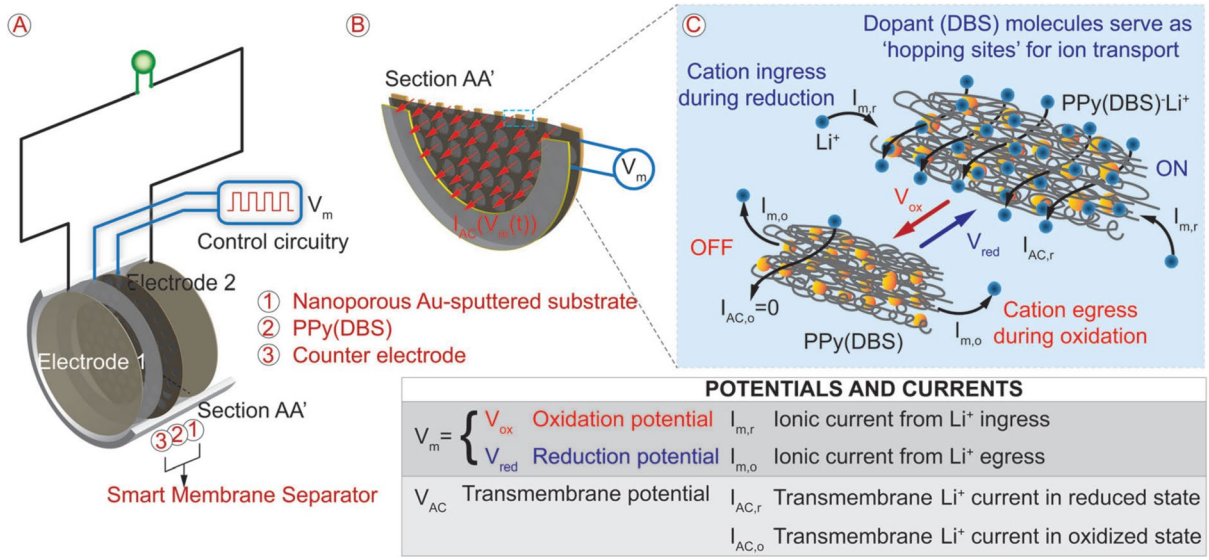

Figure 8: Dodecylbenzenesulfonate doped polypyrrole (PPy(DBS)) ionic redox transistor structure and function as a RSMS (called smart membrane separator in this figure) [7].

1.4: Research Goals

The overarching goal of this research is to develop a reliable fabrication process for three-electrode lithium-ion pouch cells with a RSMS and characterize the performance of these cells. The capability to internally and reversibly counteract thermal runaway as well as provide periods of high-power charge or discharge will be demonstrated. Cost reduction will also be pursued by exploring alternative metal substrates to gold in the construction of the RSMS.

Chapter 2: Methods

2.1: Baseline Li-ion Pouch Cells

2.1.1: Fabricating Baseline Cells

Standard two electrode pouch cells were fabricated to learn the fabrication process and serve as baseline cells to compare the charge-discharge cycling performance of the pouch cells with a RSMS to. Graphite on copper foil was used as the anode, NMC111 on aluminum foil was used as the cathode, and Celgard 2400 polypropylene was the battery separator material used. The weld tabs used were 4mm width nickel tabs and aluminum tabs. Strapping tape for pouch and cylinder cells was used as the battery tape. The battery electrolyte used was EC:DMC (1:1 w:w) with 1M $LiPF_6$. Aluminum laminated film was used for the pouch cell case. One Celgard layer in between the anode and cathode corresponds to a standard two electrode pouch cell construction. Two Celgard layers represents the additional separator layer introduced in the construction of a pouch cell with a RSMS. The process used for fabricating the two electrode pouch cells is shown in Figure 9.

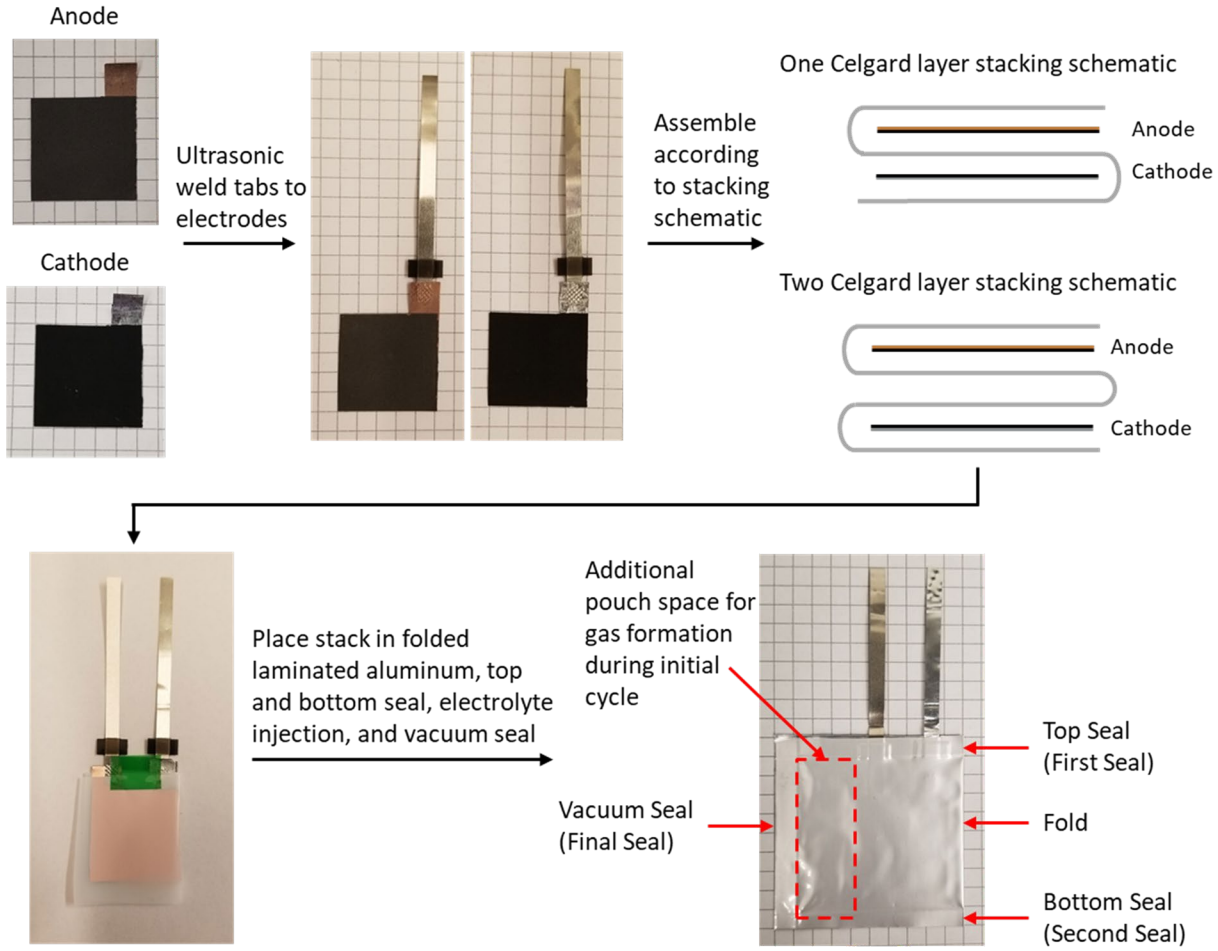

Figure 9: Baseline pouch cell fabrication process (grid sizes 0.2in x 0.2in).

The electrodes were prepared by cutting to size, 1 inch by 1 inch with a tab for welding the weld tabs to, electrode material scraped off the tabs, and weld tabs ultrasonic welded using an MTI MSK-800W ultrasonic welder to the back side of the exposed current collector tab. The tabs were cutout on the same side so that when the electrodes are facing each other the tabs will be on opposite sides. The weld tabs were chosen to be ultrasonic welded to the back side of the current collector tabs because electrode material residue would remain on the front side which would require additional steps to completely remove.

A strip of Celgard was cut sufficiently long for winding it in the corresponding stacking schematic and slightly wider than 1 inch to fully cover the electrode areas. The electrodes and Celgard were then assembled according to the stacking schematics with the electrodes aligned facing each other, battery tape was used to secure the stack, and any excess length of Celgard was cut. Laminated aluminum was then cut to size, 2 inches by 4 inches, and folded short edge to short edge with the shinier side facing inward. The electrode and separator stack and laminated aluminum were then transferred into a glove box for final assembly. With the stack inside the laminated aluminum and the edge of the stack along the fold, the tops of the weld tab melt tapes were aligned with the top edge of the laminated aluminum and sealed with the MTI MSK-115-III 3-in-1 hot sealer shown in Figure 10. The bottom edge of the laminated aluminum was then sealed with the hot sealer. 400 μL of electrolyte was injected into the pouch, worked in from the pouch exterior to facilitate wetting of stack, and the final edge was vacuum sealed. Additional pouch space was left beside the electrode and separator stack. This is traditionally temporary pouch space for gas release during the initial cycle which is punctured to release the gases, then a vacuum seal is formed next to the stack and the temporary pouch space is removed. For a single layer pouch cell this is not necessary as there is negligible release of gases during the first cycle.

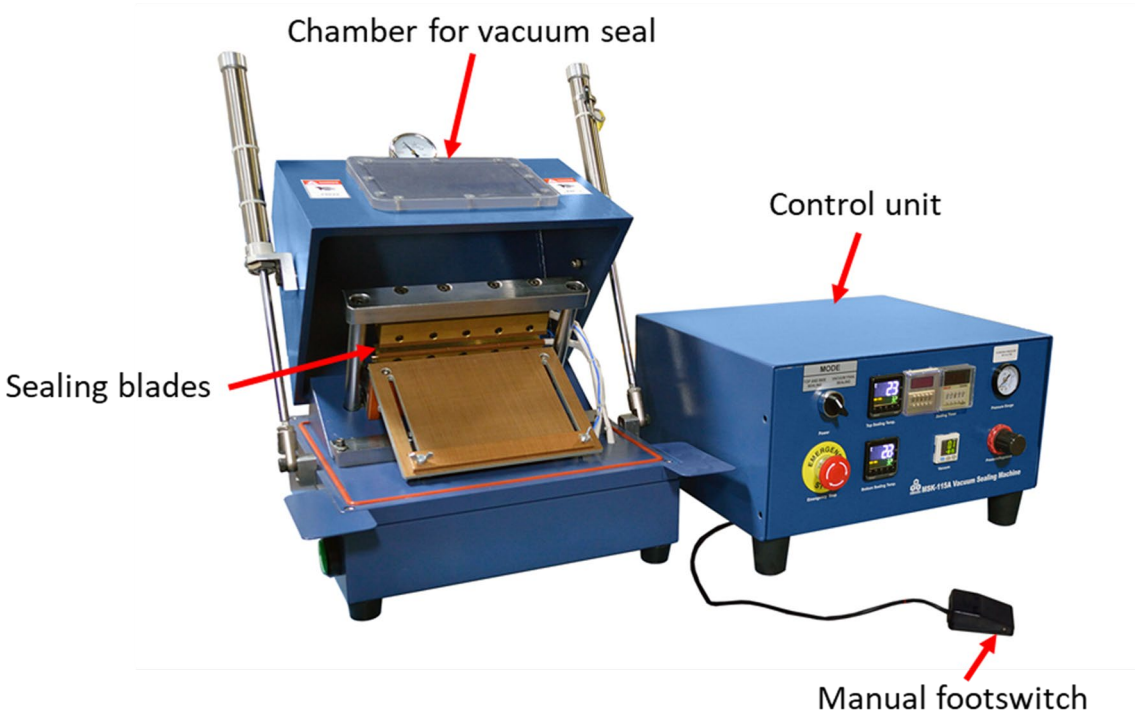

Figure 10: MTI MSK-115-III 3-in-1 hot sealer. [Source: MTI]

2.1.2: Cycle Testing Baseline Cells

The baseline pouch cells were tested using the MTI BST8-MA eight channel battery analyzer, shown in Figure 11, with charge-discharge cycling for the C-rates shown in Table 1 for potentials between 2.8V and 4.2V. The corresponding currents for a specific C-rate were calculated using Equation 1. The rated specific capacity of the cathode was 2 mAh/cm^2 and the anode was 2.4 mAh/cm^2, thus the cathode was the limiting capacity and used in the calculations for current. A C-rate of 0.775C was the max C-rate the battery tester could provide due to its max current of 10mA and the size of the pouch cell electrodes. Since newly fabricated pouch cells start in the discharged state, each cell first went through a C/12 charge, then began the cycling. A complete set of cycles consisted of four discharges and charges at each C-rate.

Figure 11: MTI BST8-MA eight channel battery analyzer. [Source: MTI]

Table 1: C-rates and the corresponding current.

C-rate	**Corresponding Current (mA)**
C/12	1.075
C/8	1.6125
C/4	3.225
C/2	6.45
0.775C	10

$$Current = Specific\ Capacity * Area * Crate \quad (1)$$

2.2: Li-ion Pouch Cells with Gold-Based RSMS

2.2.1: Fabricating Gold-Based RSMS

The fabrication of the gold-based RSMS follows the same steps as the fabrication of the RSMS used in Swagelok cells [11] which is at its core on ionic redox transistor technology [7]. The general process of RSMS fabrication is shown in Figure 12 with a PPy(DBS) electropolymerization charge density of 0.3 C/cm^2. The RSMS fabricated for the pouch cell was a square profile 1.125 by 1.125 inch with a 0.125 inch bezel around the desired electropolymerization area and a long current lead instead of the circular profile that was used in Swagelok cells.

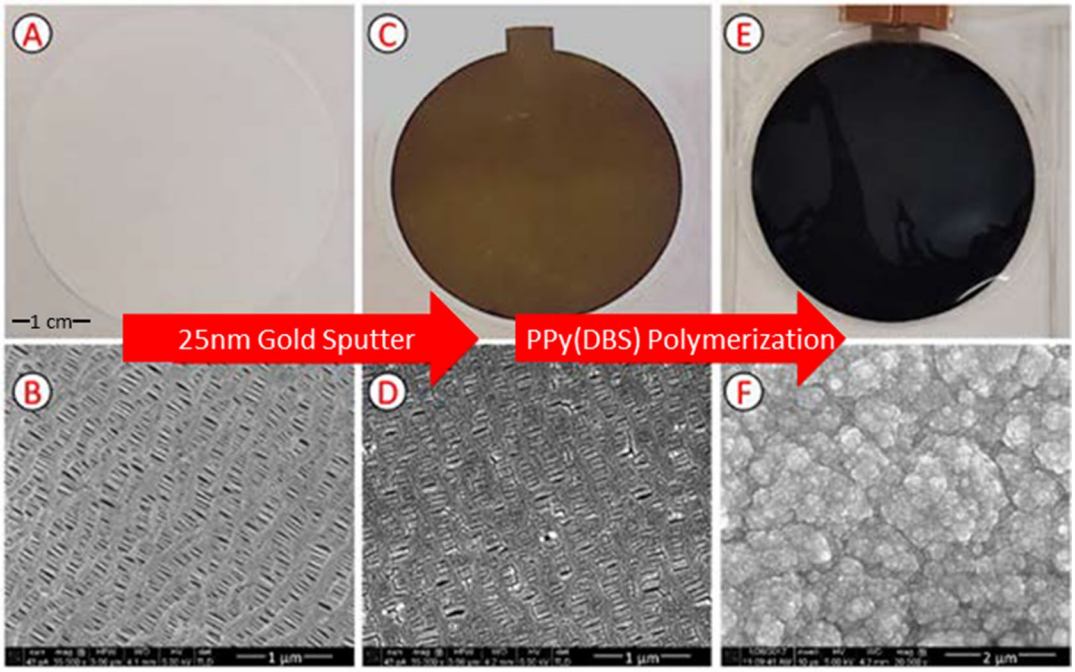

Figure 12: Membrane separator fabrication steps [11].

The RSMS shape was tailored to have a built-in current lead to provide external electrical connectivity as the gold sputtered Celgard was incompatible for ultrasonic welding with the weld tabs. Hot melt adhesive tape was added to the RSMS current lead for effective sealing along the pouch edge. The gold sputtered Celgard could not withstand the recommended melt tape parameters of 175°C at 300kPa for 3 seconds, so the parameters had to be swept through until a temperature, pressure, and time that effectively sealed the melt tape together without destroying the gold sputtered Celgard were found. The parameter testing was done on sample strips of gold sputtered Celgard. Successful parameters were determined with visual inspection of the melt tape seal formed and manually applying a small pulling force to attempt to separate the tape. Qualitative inspection was sufficient as the melt tape would undergo additional sealing with the hot seal of the top edge of the pouch during pouch cell fabrication. The RSMS with melt tape is shown in Figure 13. The bezel surrounding the electropolymerization area has been trimmed although not required.

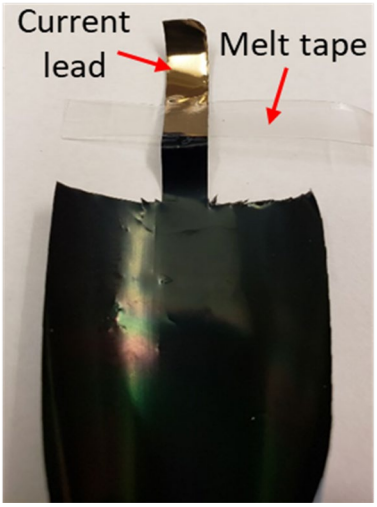

Figure 13: Fabricated gold-based RSMS with melt tape for pouch cell.

2.2.2: Fabricating Cells with Gold-Based RSMS

The fabrication process for pouch cells with a RSMS shares many of the same steps as the baseline pouch cells. The electrodes were prepared the same as for the baseline pouch cells. Incorporating the RSMS, prepared as described in the previous section, into the stack was the main difference compared to the baseline cells. The melt tape on the RSMS current lead was trimmed to fit between the melt tapes of the electrode weld tabs. A strip of Celgard was cut sufficiently long for winding it in the stacking schematic and slightly wider than 1.125 inches to fully cover the RSMS active area. The fabrication process starting from the stacking step is shown in Figure 14. The electrodes, RSMS, and Celgard were then assembled according to the stacking schematic with the electrodes aligned facing each other, centered with the RSMS active area, and the RSMS active area facing the anode. A layer of Celgard was added in between the active area of the RSMS and anode to prevent an electrical short between the RSMS and Li^+ SEI. The back side of the RSMS, facing the cathode, was plain Celgard so an additional layer was not needed in between. In the single layer pouch cells created by hand, the RSMS was a separate component from the Celgard strip wound in the stacking schematic. In a roll-to-roll process for mass production, the RSMS would be part of the Celgard strip wound through the anode and cathode. With the stack including the RSMS complete, the laminated aluminum pouch preparation, electrolyte injection, and sealing were performed the same as the baseline pouch cells.

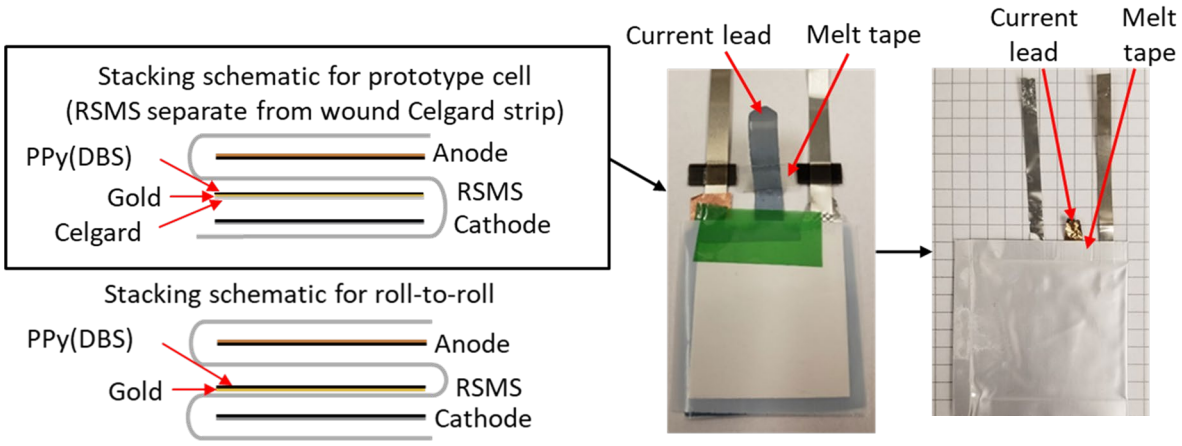

Figure 14: RSMS stacking schematics, stack, and finished pouch cell (grid size 0.2in x 0.2in).

2.2.3: Characterization of Cells with Gold-Based RSMS

The charge-discharge cycling of the cells with the gold-based RSMS were performed similar to the cycling of the baseline cells. For steady-state charge-discharge cycling of the cell, the RSMS could be placed in the reduced or oxidized state. A complete set of cycles for a given redox state consisted of C/12 and C/4 C-rates which was performed with the membrane in the reduced state then repeated with the membrane in the oxidized state for multiple sets of cycles. After each set of cycles for a given membrane redox state, cyclic voltammetry was performed to monitor the membrane health, then chronoamperometry was performed to place the membrane in the desired redox state for the next set. Cyclic voltammetry and chronoamperometry were performed using the Ivium Technologies pocketSTAT, shown in Figure 15, as a potentiostat. In between some of the sets of cycles with the membrane in the reduced then oxidized states, real-time tests were performed in which the RSMS was reduced or oxidized versus the anode or cathode during a charge or discharge.

Figure 15: Ivium Technologies pocketSTAT. [Source: Ivium Technologies]

The circuit diagram for the setup of the real-time tests is shown in Figure 16. The components are the battery tester, the pouch cell with its cathode (+), RSMS (dashed line), and anode (-), and the potentiostat (PSTAT). The diagram on the left with the potentiostat connected to the RSMS and anode is the circuit for redox events of the membrane versus the anode. The diagram on the right with the potentiostat connected to the cathode and RSMS is the circuit for redox events of the membrane versus the cathode.

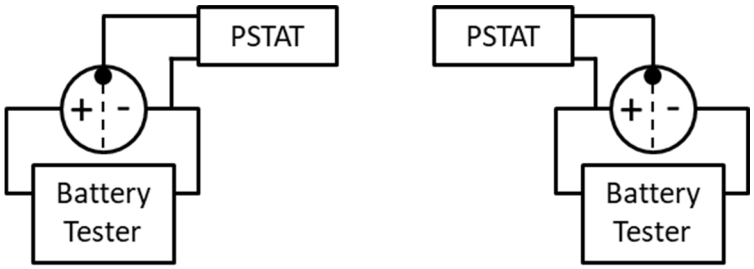

Figure 16: Circuit diagram for real-time tests.

Figure 17 on the next page shows the charging circuit diagram with the membrane in open circuit on the left and membrane reduction versus the anode on the right. This real-time mode is desirable for counteracting thermal runaway. Thermal runaway during charging of a

battery typically begins at the anode so removing the current at the anode is desired to halt these reactions. More details on thermal runaway can be found in Section 1.1. Membrane reduction versus the anode achieves this by actively depleting Li^+ ions at the anode and diverting the charging current through the membrane, effectively shutting down the charging of the battery for a period. Also, with the anode as the counter/reference electrode no additional energy was required for the membrane reduction. The real-time test was performed by starting with the pouch cell discharged, then a one-hour charging cycle was initiated with the membrane in open circuit. During charging, the membrane was reduced versus the anode by diverting current from the battery tester through the membrane. After the reduction event was complete, the membrane was returned to open circuit and the charging cycle continued. This test was performed for both a constant voltage charge at 4V and a constant current charge of C/4.

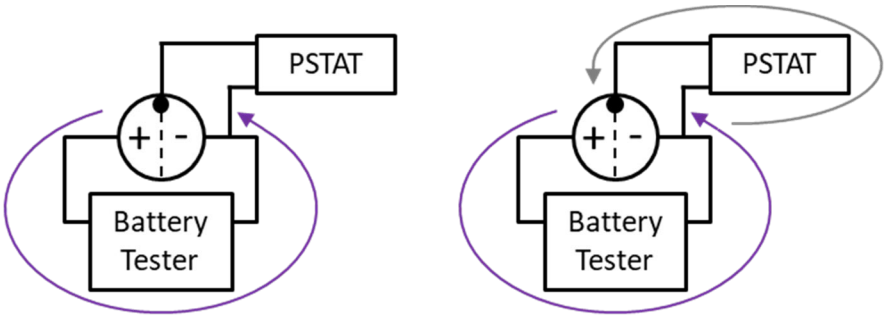

Figure 17: Charging circuit diagram for membrane reduction versus the anode.

Figure 18 and Figure 19 show the discharging circuit diagrams for real-time tests of providing periods of higher power discharge. These real-time modes are desirable for providing additional power during events such as take-offs and accelerations. Figure 18 on the next page shows the discharging circuit diagram with the membrane in open circuit on the left and membrane oxidation versus the anode on the right. Membrane oxidation versus the anode

enables higher power discharge by providing excess Li^+ ions at the anode. This results in a decreased anode current and increased cathode current providing a burst of additional current that can be used by the load. The real-time test was performed by starting with the pouch cell charged, then a one-hour C/4 constant current discharge cycle was initiated with the membrane in open circuit. During discharging, the membrane was oxidized versus the anode by passing current from the membrane through the control circuitry. After the oxidation event was complete, the membrane was returned to open circuit and the discharging cycle continued.

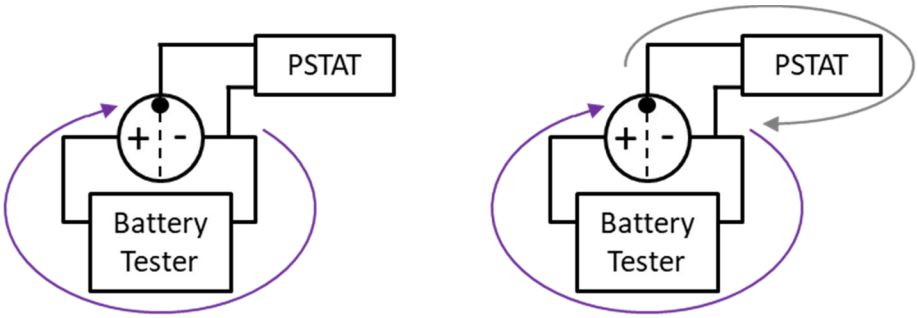

Figure 18: Discharging circuit diagram for membrane oxidation versus the anode.

Figure 19 on the next page shows the discharging circuit diagram with the membrane in open circuit on the left and membrane reduction versus the cathode on the right. Membrane reduction versus the cathode enables higher power discharge by depleting Li^+ ions at the cathode. This results in an increased anode current and decreased cathode current providing a burst of additional current that can be used by the load. The real-time test was performed by starting with the pouch cell charged, then a one-hour 715Ω constant resistance discharge cycle was initiated with the membrane in open circuit. A constant resistance discharge was used to demonstrate both the discharging current and voltage could increase, since the battery tester

could not provide a constant voltage discharge. During discharging, the membrane was reduced versus the cathode by diverting current from the cathode through the membrane. After the reduction event was complete, the membrane was returned to open circuit and the discharging cycle continued. Unlike membrane reduction versus the anode during charging, some energy input is required for membrane oxidation versus the anode or reduction versus the cathode during discharging.

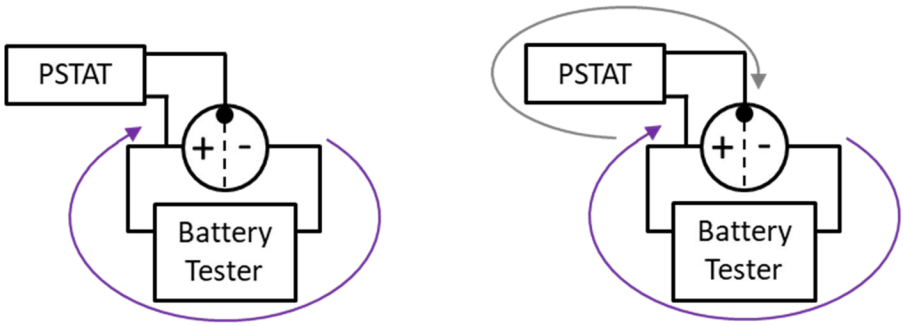

Figure 19: Discharging circuit diagram for membrane reduction versus the cathode.

2.3: Alternative Metals for RSMS Cost Reduction

The RSMS made with gold would quickly become cost prohibitive for production as passive membrane separators account for approximately 26% of standard lithium-ion cell cost, so a cheaper alternative metal in the fabrication is desired [12]. Alternative metals explored were aluminum, nickel, and each with a top layer of titanium added. Aluminum and nickel were chosen due to their low cost, traditional use in lithium-ion batteries, and stability in electrolyte at the potentials the RSMS would be operating at. Aluminum sputter targets are around 6.1 times cheaper and nickel sputter targets are around 4.7 times cheaper than gold [Source: Ted Pella]. A top layer of titanium on both aluminum and nickel was explored because findings in literature showed the titanium oxide layer formed is highly conductive and thus desirable for

electropolymerization [13]. These metals were deposited on Celgard using the AJA Orion RF/DC Sputter Deposition Tool in the cleanroom at Ohio State's Nanotech West Laboratory. After deposition, SEM images were taken to ensure the Celgard pores were not covered up by the thickness of metal deposited. Strips of each metal sputtered Celgard were cut and electropolymerization trials were done with the setup shown in Figure 20. Solutions of 0.2M to 0.6M pyrrole and 0.1M NaDBS at potentials of 0.5V to 0.75V were used for the trials. Cyclic voltammetry was performed with the setup shown in Figure 21 on the most promising electropolymerized samples to examine the redox behavior and filling efficiency of the samples.

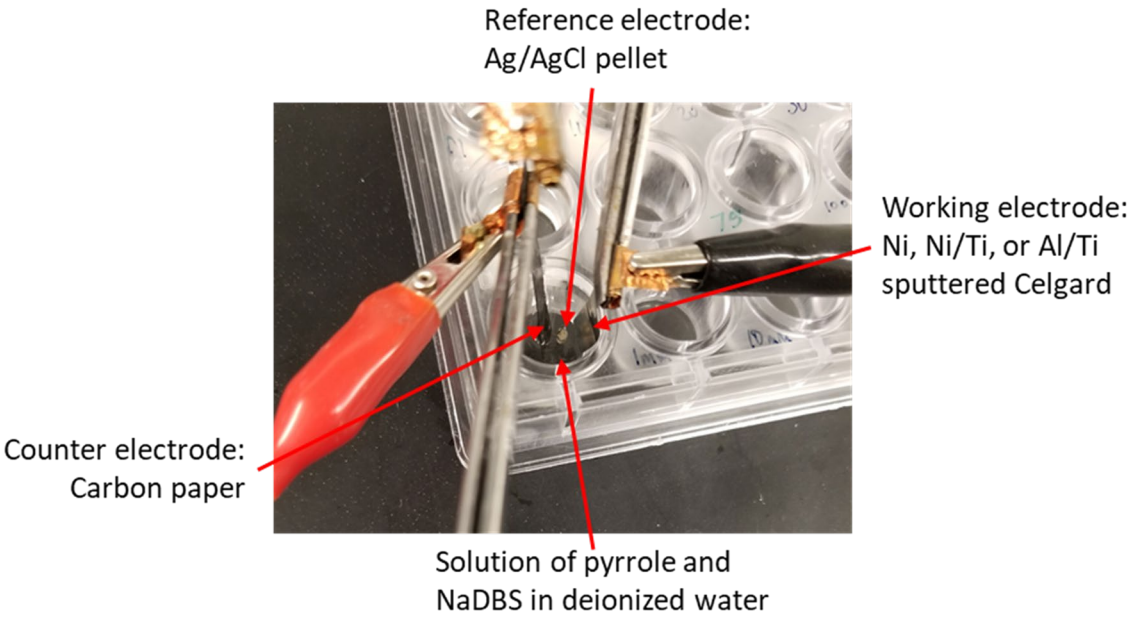

Figure 20: Setup for electropolymerization trials.

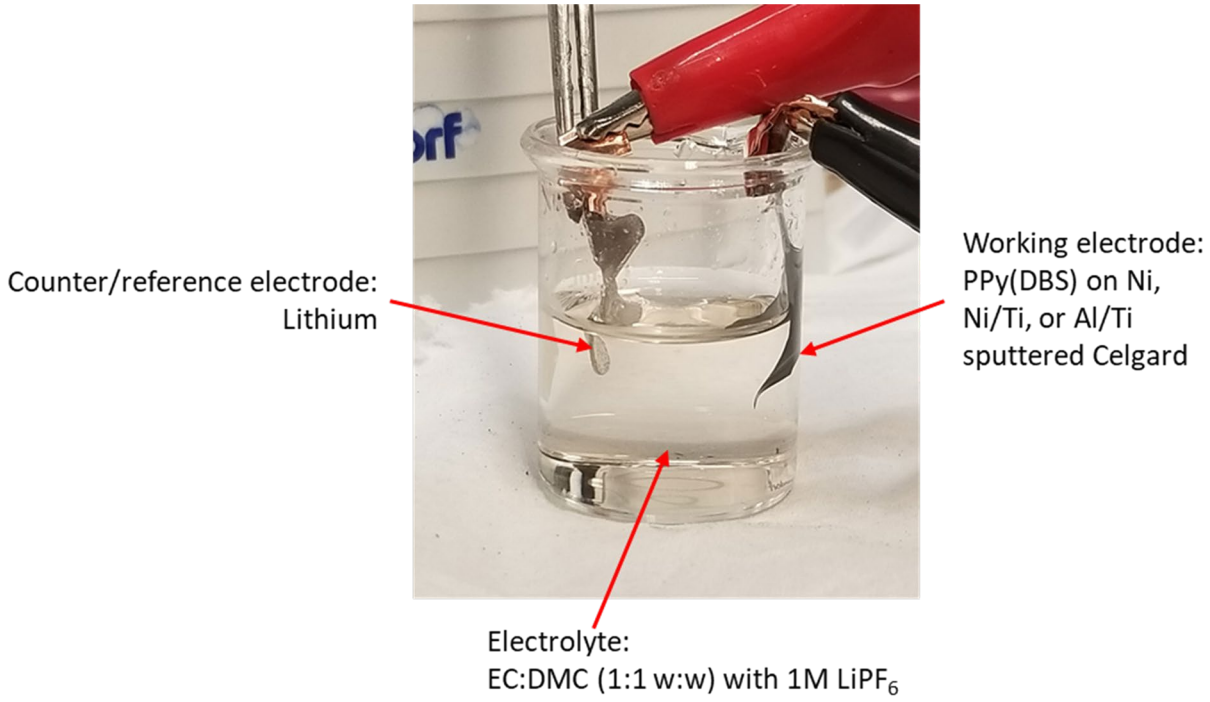

Figure 21: Cyclic voltammetry setup for electropolymerized samples.

2.4: Li-ion Pouch Cells with Nickel-Based RSMS

2.4.1: Fabricating Nickel-Based RSMS

To create a nickel-based RSMS, first the nickel deposition would have to be in the desired pattern. To achieve this, a mask was made with 3 cutouts of the desired pattern out of 304 stainless steel. The deposition pattern was the same dimensions as the pattern for the gold-based RSMS. The material used for the mask had to be cleanroom approved material, thus 304 stainless steel was used. To increase the consistency between RSMS cutouts, laser cutting was preferable. An Epilog Laser Fusion 75W CO_2 laser cutter in the Scott Laboratory Research Shop was used to laser cut the Celgard profiles. A speed of 14 percent, power of 4 percent, and frequency of 40 percent were used.

To aid in alignment and hold the Celgard flat for laser cutting, a die was also made from 304 stainless steel. The mask and die cutouts were made with a waterjet cutter, shown in Figure 22, in the Baker Systems Engineering Machine Shop. The dimensions for these parts are given in their drawings in Appendix A in Figure A1 and Figure A2.

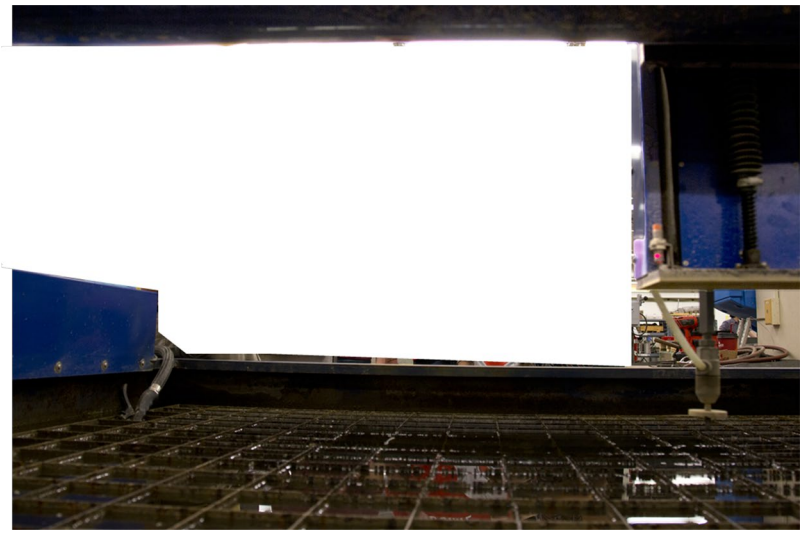

Figure 22: Waterjet Cutter.

The finished mask and die are shown below in Figure 23. For depositing nickel, Celgard was placed behind the mask on the sputter stage. The deposition is shown with the mask and Celgard still on the sputter stage on the left and the mask removed on the right in Figure 24. The die, Celgard, and mask stacked for laser cutting is shown in Figure 25 on the left and the laser cut profiles on the right.

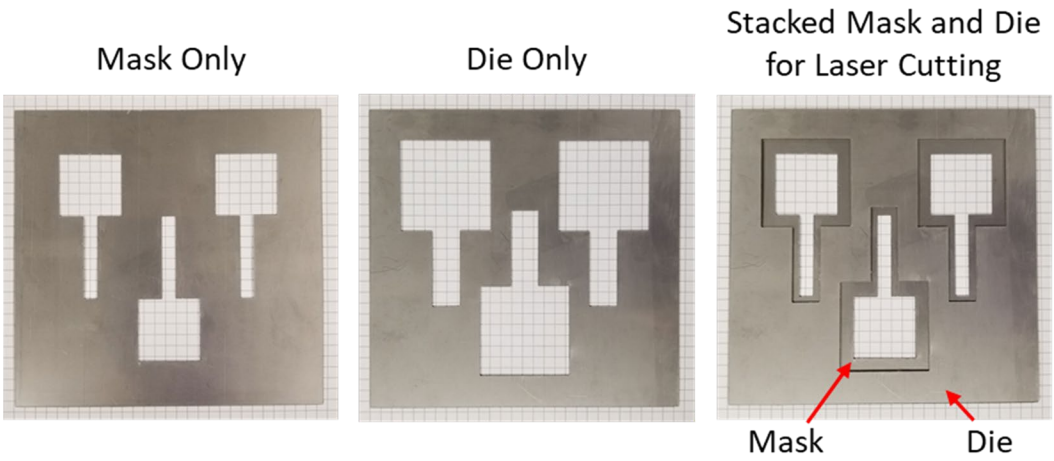

Figure 23: Mask and die pictured separately and stacked (grid sizes 0.2in x 0.2in).

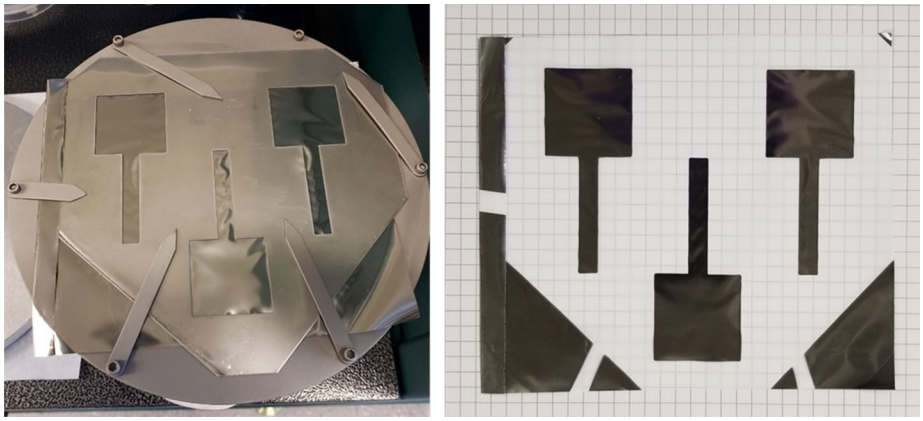

Figure 24: Images after nickel deposition on Celgard (grid size 0.2in x 0.2in).
(note the mask corners were trimmed to fit on sputter stage)

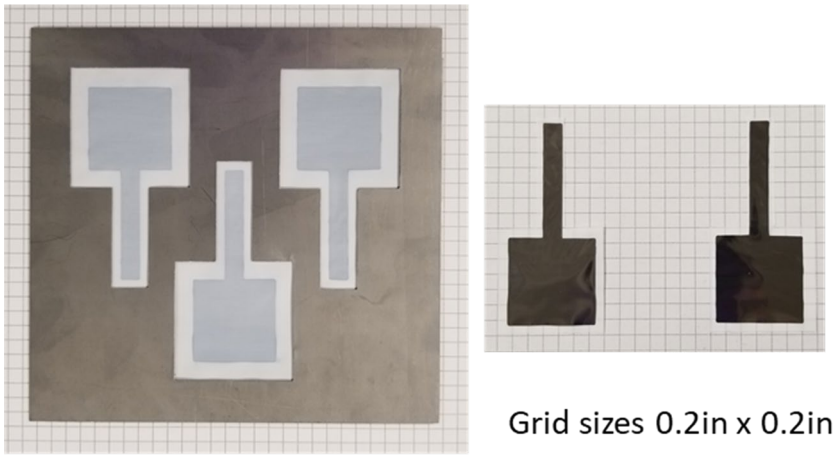

Figure 25: Die, nickel sputtered Celgard, and mask stacked together for laser cutting (left) and laser cut out profiles (right).

The PPy(DBS) electropolymerization for the nickel-based RSMS was performed the same as for the gold-based RSMS. The nickel-based RSMS is shown in Figure 26 before PPy(DBS) electropolymerization on the left and after electropolymerizing PPy(DBS) to a charge density of 0.3 C/cm^2 on the right. Melt tape was added to the nickel-based RSMS as well, shown in Figure 27.

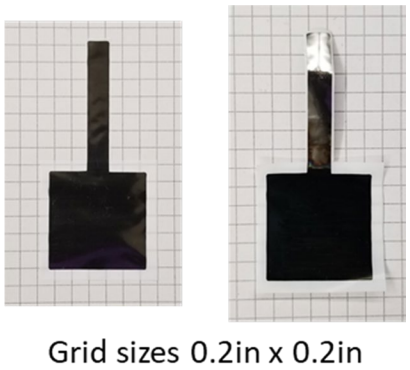

Figure 26: Nickel-based RSMS before and after PPy(DBS) electropolymerization. (note this first sample was cut by hand)

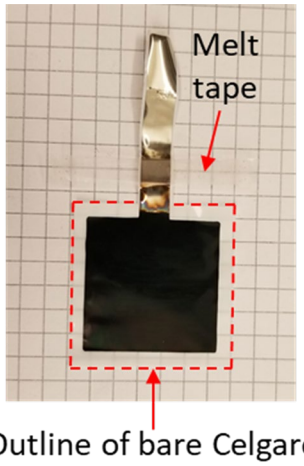

Figure 27: Fabricated nickel-based RSMS with melt tape for pouch cell (grid size 0.2in x 0.2in).

2.4.2: Fabricating Cells with Nickel-Based RSMS

Pouch cells with a nickel-based RSMS were fabricated the exact same way as with the gold-based RSMS, the only difference being the type of RSMS included in the stack. The stack with the nickel-based RSMS is shown in Figure 28 on the left and the finished pouch cell on the right.

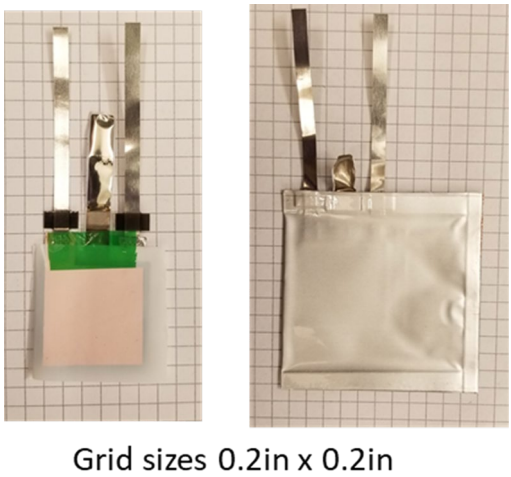

Figure 28: Stack with nickel-based RSMS (left) and finished pouch cell (right).

2.5: Conclusions

In this chapter, the fabrication methods for baseline pouch cells and the RSMS were investigated. The necessary changes for reliably fabricating a pouch cell with a gold-based RSMS were developed. Charge-discharge cycling was performed on the baseline cells and the cell with a gold-based RSMS for comparison. Real-time testing of the pouch cell with the gold-based RSMS was performed to verify the shutdown and power boost capabilities. For cost reduction, alternative metals to gold in the fabrication of the RSMS were explored. The fabrication process was developed for a nickel-based RSMS, one of the alternatives to gold, and a pouch cell with this RSMS.

Chapter 3: Results

3.1: Baseline Pouch Cells

The baseline pouch cell cycle data for 1 Celgard layer is shown in Figure 29. The left y-axis and blue data are the specific capacity, the right y-axis and red data are the specific energy. The dashed black line at a specific capacity of 160 mAh/g is the theoretical maximum specific capacity of the cell, since the cathode's rated specific capacity of 160 mAh/g was the limiting specific capacity. As the C-rate increased from C/12 to 0.775C the capacity drops, which is typical of simply increasing the C-rate. The specific capacity and energy gradually decreased as the cell was cycled, which again is typical of batteries. Note cycles 41 through 240 are omitted in the plot to show the difference in capacity for the beginning cycles versus hundreds of cycles later. The baseline cell with 1 Celgard layer was made first and went through 280 cycles to examine the degradation of single layer pouch cells able to be fabricated. The capacity for C/12 was approximately 67% and 0.775C was approximately 55% of the initial capacity.

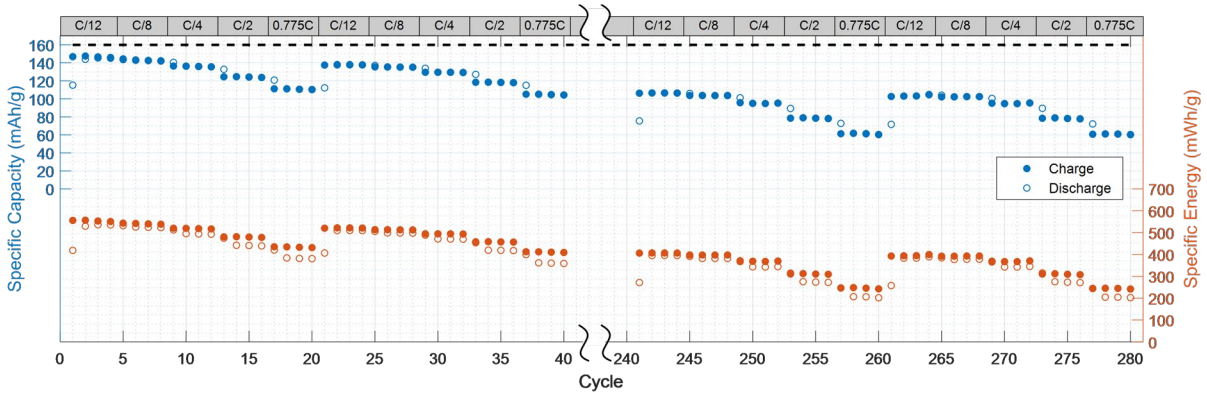

Figure 29: Cycle data for baseline pouch cell with 1 Celgard layer.

The cycle data for the baseline cell with 2 Celgard layers is shown in Figure 30. The capacities are very comparable to the cell with 1 Celgard layer, which suggests the additional Celgard layer has little impact. The initial set of cycles for the cell with 2 Celgard layers are slightly lower than the cell with 1 Celgard layer for the lower C-rates, and slightly higher for the higher C-rates. The capacity of the cell with 2 Celgard layers slightly increases over some of the C-rates in the first set of cycles and starts out greater for the second set of cycles. This could be due to the separators and electrodes not being fully wetted by the electrolyte initially and subsequently wetted during the initial cycles. Variation in the actual specific capacity of the electrodes can also contribute to differences between different pouch cells. Electrode sheet specific capacities are based on the average from a large sheet of the electrode, so individual cutouts from the sheet could slightly vary. Also, the cutouts were done by hand for these cells so small variations in size could also be present.

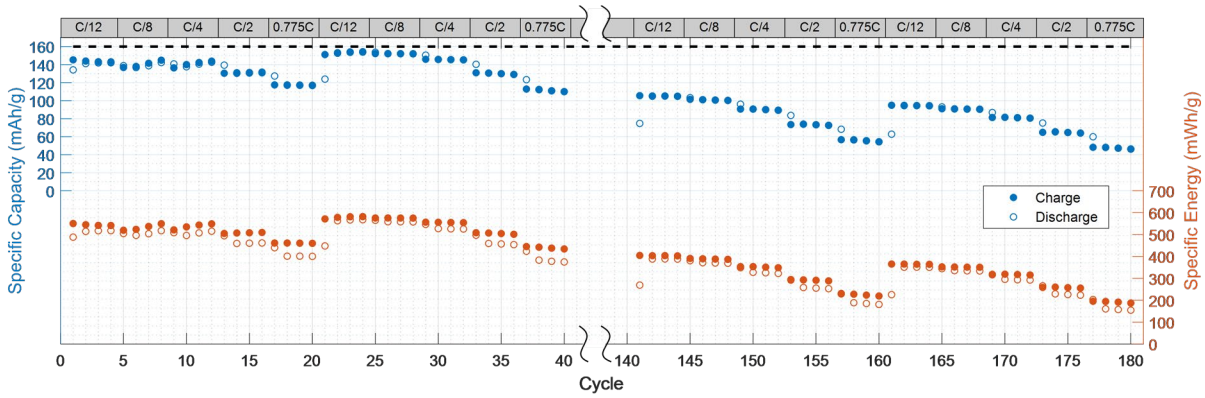

Figure 30: Cycle data for baseline pouch cell with 2 Celgard layers.

3.2: Gold-Based RSMS Pouch Cell

3.2.1: Melt Tape Parameters

As discussed in section 2.2.1, the melt tape sealing temperature, pressure, and time had to be swept through to find the optimal temperature, pressure, and time as shown in Table 2 on the next page. First the temperature was stepped down from the manufacturer recommended parameters in trial 1. For trial 2 the temperature and pressure were both stepped down, with the pressure the minimum required for the melt press to clamp together. The melt tape did not seal, so the time was increased up to 120 seconds. Longer than 120 seconds was not desirable, so the temperature was increased until the minimum required to effectively seal the melt tape. To obtain a faster sealing time, the temperature was further increased and then the pressure was increased up to the manufacturer recommended pressure. Once the temperature of 130°C and pressure of 300kPa were found to be optimal, the time was further adjusted to find the optimal sealing time of 15 seconds.

Table 2: Melt tape trials sweeping through temperature, pressure, and time to find parameters for effective sealing without destroying RSMS.

Trial	Temperature (°C)	Pressure (kPa)	Time (s)	Result
Manufacturer Recommended	175	300	3	Melted sample
1	145	300	5	Melted sample
2	115	Min	5	Failed adhesion
3	115	Min	20	Failed adhesion
4	115	Min	120	Failed adhesion
5	118	Min	120	Failed adhesion
6	121	Min	120	Failed adhesion
7	125	Min	120	Failed adhesion
8	128	Min	120	Successful
9	128	100	60	Minimal adhesion
10	135	100	20	Minimal adhesion
11	135	300	10	Successful
12	130	300	10	Medium adhesion
13	130	300	20	Successful
14	130	300	15	Successful

3.2.2: Charge-Discharge Cycles

The pouch cell with the gold-based RSMS cycle data is shown in Figure 31. The membrane was in the reduced state throughout the green portions of the plot and was in the oxidized state throughout the red portions. The vertical dashed green or red lines indicate when a cyclic voltammetry and chronoamperometry was done on the membrane. Each cyclic voltammetry was performed to ensure the membrane continued to exhibit the desired redox behavior and each chronoamperometry was performed to place the membrane in the desired redox state for the following cycles. The capacity of the cell for C/12 with the membrane in the reduced state was comparable to the baseline cells. For C/4 with the membrane in the reduced state the capacity was lower than the baseline cells. The capacities of the cell with the membrane in the oxidized state were lower than the reduced state, with a greater decrease for C/4. The

decrease in capacity from the addition of the RSMS is due to some additional internal resistance faced by the ion transport through the membrane. The difference was greater for the oxidized state since there is cation egress from the membrane during oxidation resulting in the membrane being less open.

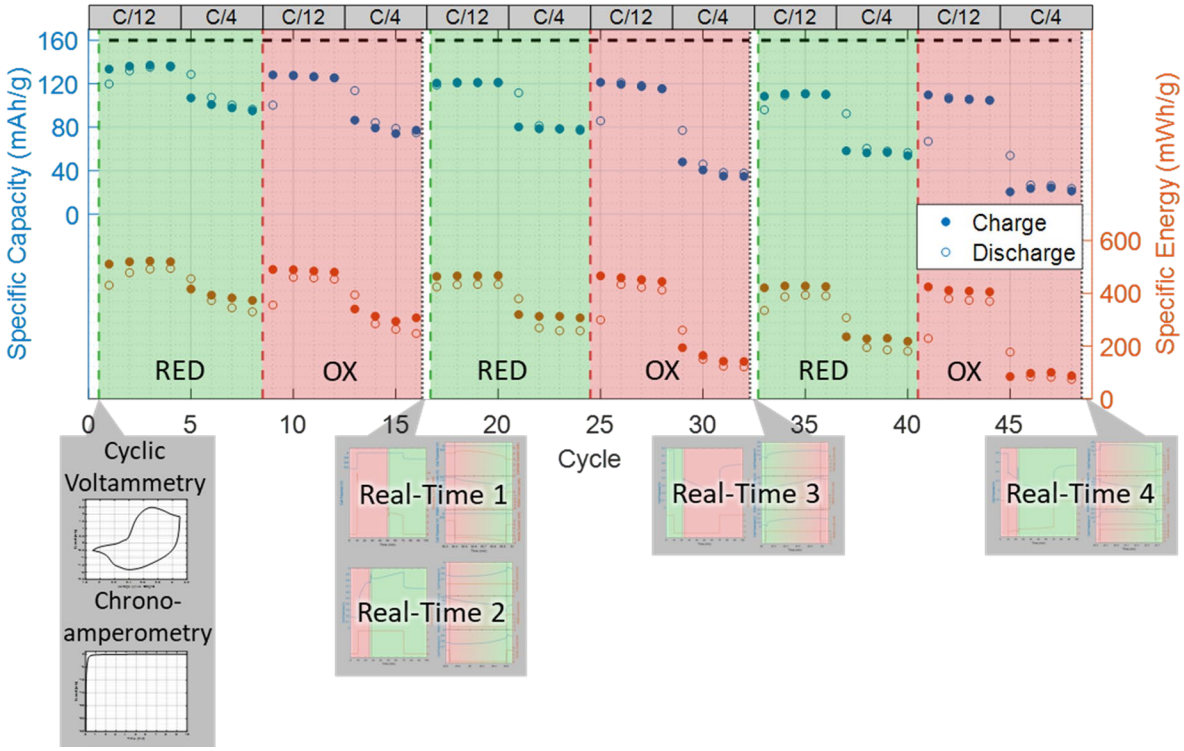

Figure 31: Charge-discharge cycle data for pouch cell with gold-based RSMS in reduced and oxidized states.

The vertical dotted black lines indicate when real-time testing was done with the pouch cell. Before each real-time test, cyclic voltammetry was performed as was the case for the vertical dashed green or red lines. Between cycles 16 and 17, real-time tests 1 (constant voltage charge) and 2 (constant current charge) were performed. Between cycles 32 and 33, real-time test 3 (constant current discharge) was performed. After cycle 48, real-time test 4 (constant resistance discharge) was performed. These real-time tests are further discussed in the next section.

The first cyclic voltammetry is shown in Figure 32. The desired redox behavior of the membrane is a clear oxidation and reduction peak. The oxidation peak can be seen around 2.7V for the sweep with increasing voltage, and the reduction peak can be seen around 2.4V for the sweep with decreasing voltage.

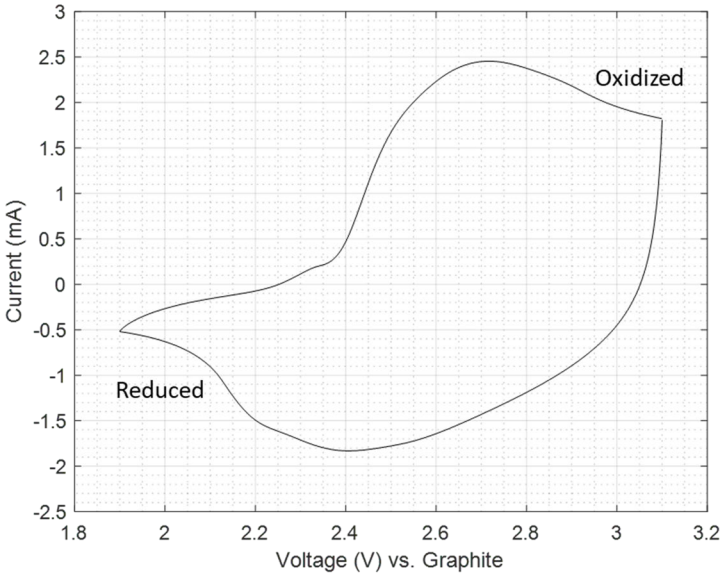

Figure 32: First cyclic voltammetry of gold-based RSMS.

The first chronoamperometry shown in Figure 33 on the left was performed after the cyclic voltammetry to place the membrane in the desired redox state. The desired redox state in this case was the reduced state, so the chronoamperometry was performed at 2V, a voltage past the reduction peak. The reducing current starts out large and quickly approaches zero, which indicates the membrane is approaching the fully reduced state. The current will never actually reach zero, so the chronoamperometry was stopped once a current on the order of μA was achieved. The corresponding charge movement compared to the maximum theoretical charge movement of the RSMS is shown in Figure 33 on the right, which has a negative sign due to ion ingress into the RSMS. If placing the membrane in the oxidized state was desired, the

chronoamperometry would be performed at a voltage past the oxidation peak, and the oxidizing current would be decreasingly positive instead of decreasingly negative for the reducing current.

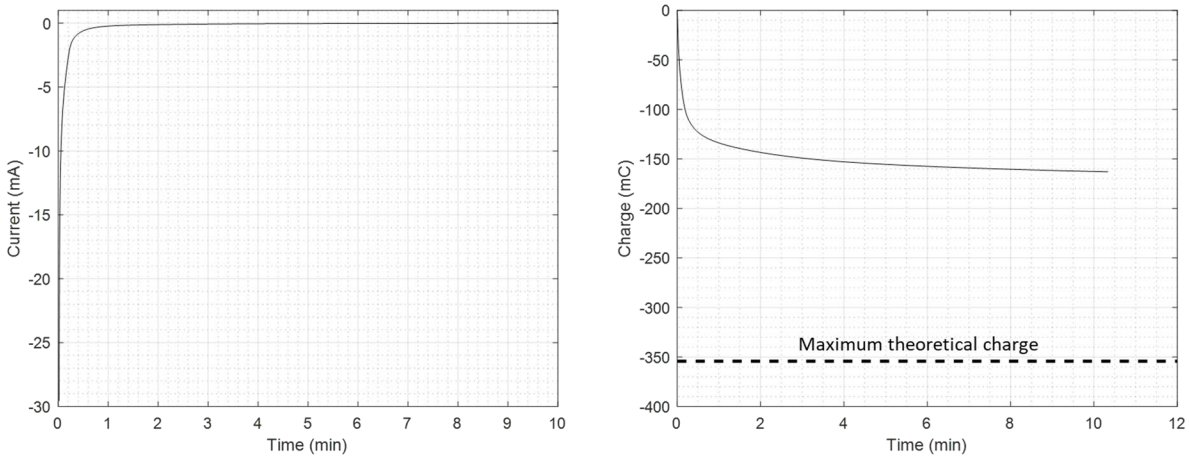

Figure 33: First chronoamperometry to place the membrane in the reduced state (left) and the corresponding negative charge from ion ingress compared to the theoretical maximum (right).

3.2.3: Real-Time Tests

Each of the real-time tests performed are described in section 2.2.3. The first real-time test, constant voltage charge with a membrane reduction event versus the anode, is shown in Figure 34. The cathode and RSMS currents were directly measured by the battery tester and potentiostat respectively. The anode current was calculated using Kirchhoff's current law. During the reduction event, the anode current decreased and became negative which means the cell was discharging during this period. This was due to an overestimation of how much current the battery tester would provide during the reduction event, thus more current than necessary was diverted through the RSMS. The reduction in anode current showed the RSMS was able to effectively shut down the charging of the cell by removing current at the anode for just over 30 seconds, which would be desirable in the event of thermal runaway. The total charge transferred by the RSMS during the reduction event was 158.1 mC, calculated with Equation 2.

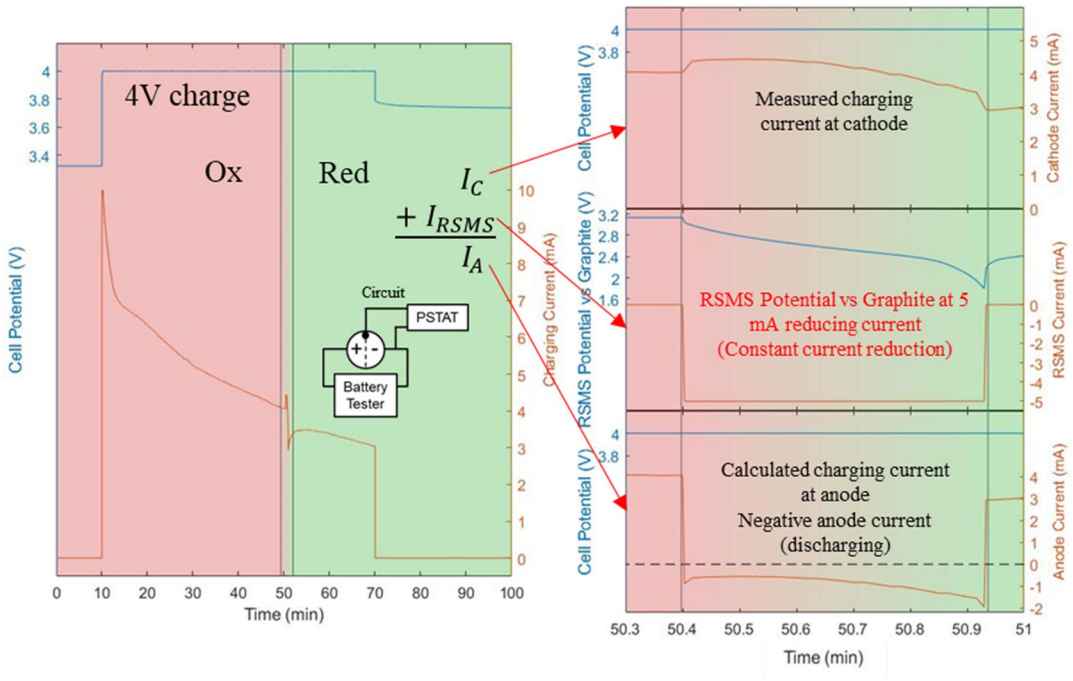

Figure 34: Real-time 1 – constant voltage charge with a RSMS reduction versus anode.

$$Q = \int_{t_i}^{t_f} i \, dt \tag{2}$$

The second real-time test was also to demonstrate the ability of the RSMS to shut down the charging of the cell in the event of thermal runaway, but this test was performed as a constant current charge with a membrane reduction event versus the anode, shown in Figure 35. With a constant current charge, the exact amount of current to divert through the RSMS was known. During the reduction event, the anode current dropped to zero signifying the charging of the cell had been effectively shut down by removing current at the anode. The reduction event lasted approximately 60 seconds and the RSMS transferred a total charge of 180.1 mC. The RSMS was able to maintain the reduction event longer and transfer more charge before reaching the cutoff voltage as less current was diverted through.

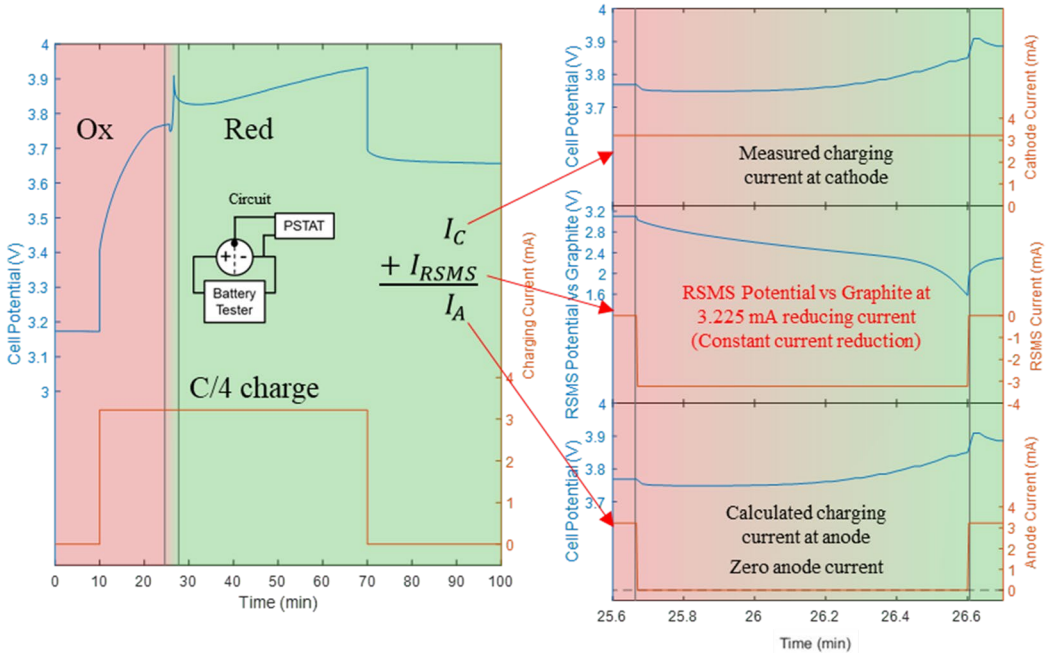

Figure 35: Real-time 2 – constant current charge with a RSMS reduction versus anode.

The third real-time test was a constant current discharge with a membrane oxidation versus the cathode shown in Figure 36. This real-time test was to demonstrate high power discharge capabilities. During the oxidation event, the discharging current at the anode was reduced to zero and the cell potential increased while discharging current was constant. This demonstrates that the anode capacity was conserved during the oxidation event and higher power discharge was provided since the potential increased and current remained the same. The oxidation event lasted just under 60 seconds and the RSMS transferred a total charge of 173.0 mC. After the oxidation event, the voltage did not follow a similar trend as before the event. This suggests there was a large steady-state effect from the membrane, which was now in the oxidized state.

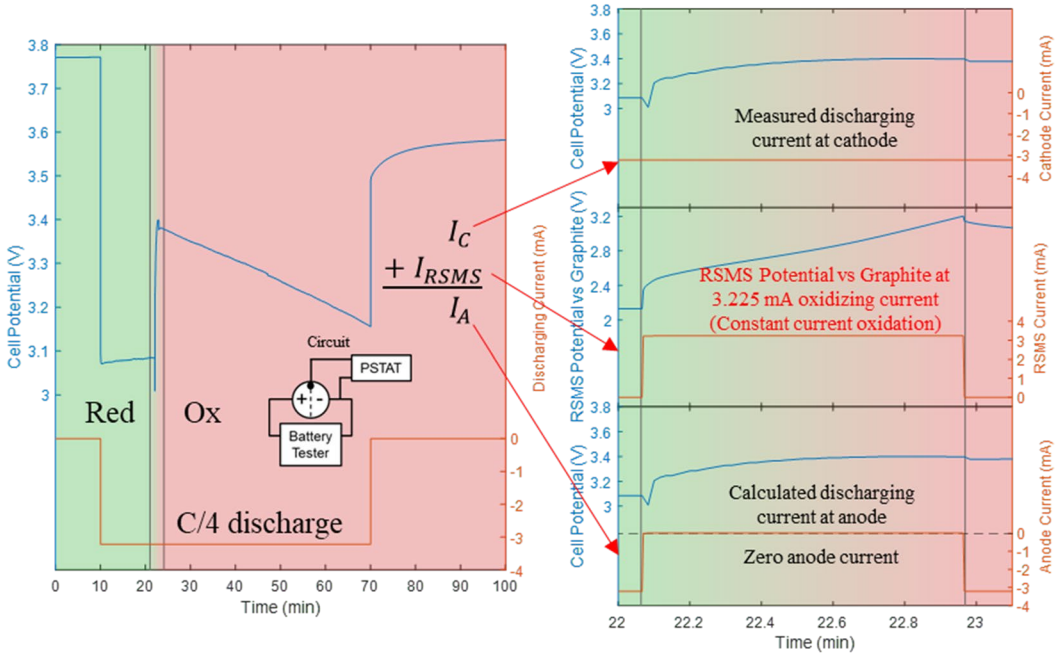

Figure 36: Real-time 3 – constant current discharge with a RSMS oxidation versus anode.

The fourth real-time test was a constant resistance discharge with a membrane reduction versus the cathode shown in Figure 37. This real-time test was also to demonstrate high power discharge capabilities, but with both the voltage and current changing. The anode and RSMS currents were directly measured by the battery tester and potentiostat respectively. The cathode current was calculated using Kirchhoff's current law. During the reduction event, the cathode current was significantly reduced and the magnitude of the current and voltage increased. This demonstrates that the cathode capacity was conserved during the reduction event and higher power discharge was provided since the potential and current magnitude both increased. The reduction event lasted just over 60 seconds and the RSMS transferred a total charge of 207.9 mC.

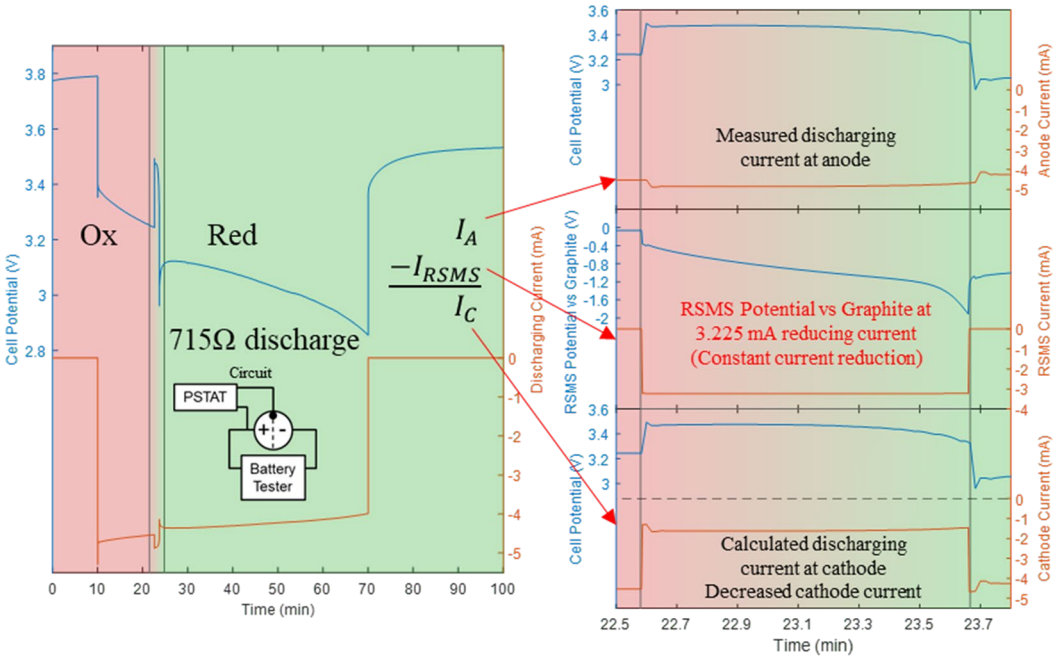

Figure 37: Real-time 4 – constant resistance discharge with a RSMS reduction versus cathode.

3.3: Alternatives Metals to Gold for RSMS

Blank Celgard, gold sputtered on Celgard, and the alternative metals sputtered on Celgard scanning electron microscopy (SEM) images are shown in Figure 38. It is important to note that a deposition with a total thickness of 50nm as measured with the AJA Orion deposition tool was comparable to a deposition of 25nm for the old sputter tool used for the gold sputtered Celgard. Images of the electropolymerization trials on the strips cut from these samples are shown in Figure 39. The ideal electropolymerization parameters are the same as gold at 0.2M pyrrole, 0.1M NaDBS, and 0.5V. Only nickel sputtered Celgard was successfully electropolymerized with those parameters. A successful electropolymerization was visually determined as a full, even layer of PPy(DBS). Circled in red are examples of unsuccessful trials with exposed metal. The samples boxed in green were deemed successful.

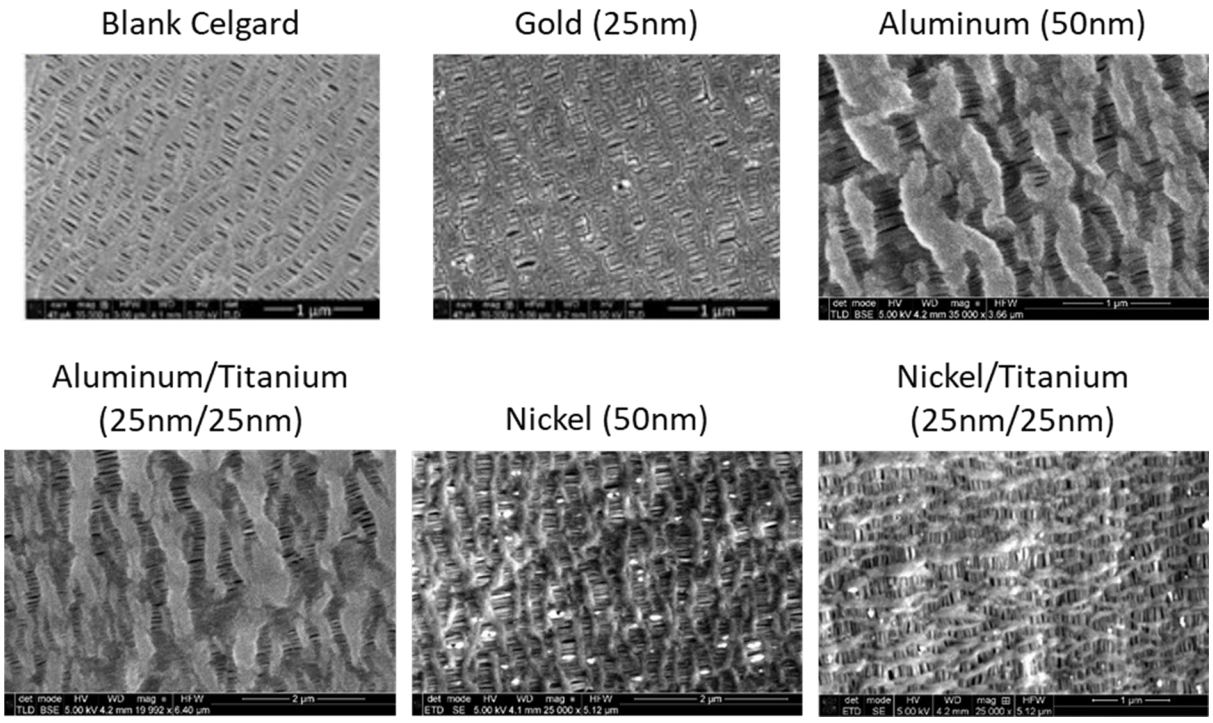

Figure 38: SEM images of blank Celgard and various metal depositions on Celgard.

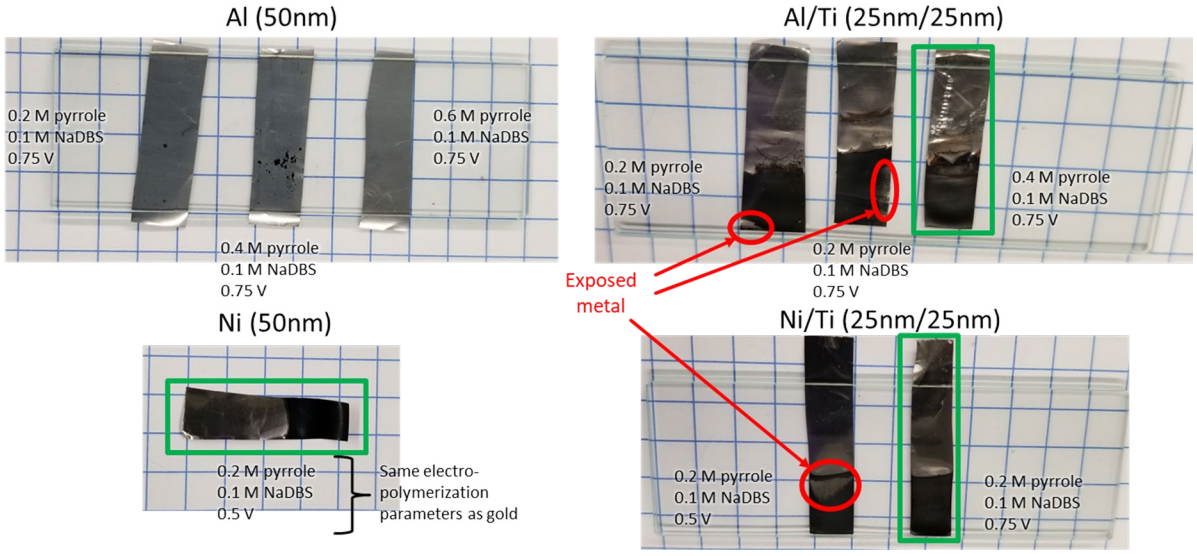

Figure 39: Electropolymerization trial results.

Results of the cyclic voltammetry performed on the successful PPy(DBS) electropolymerization samples are shown in Figure 40, Figure 41, and Figure 42. Areal charge density and filling efficiency are noted for each sample and compared to the gold-based RSMS areal charge density of 0.3C/cm^2 and filling efficiency of 42.0%. Areal charge density is the total charge movement during electropolymerization divided by electropolymerized area. Filling efficiency is calculated using Equation 3 and 4 below. In the calculation of maximum theoretical charge, the total electropolymerization charge is divided by 7 since there are 3 pyrrole monomers (losing 2 electrons each) per DBS^- (an additional electron is lost for balancing DBS^-) during electropolymerization [14].

$$Maximum\ Theoretical\ Charge = \frac{Total\ Electropolymerization\ Charge}{7} \quad (3)$$

$$Filling\ Efficiency = \frac{Actual\ Charge\ Movement}{Maximum\ Theoretical\ Charge} * 100\% \quad (4)$$

The cyclic voltammetry of the PPy(DBS) on nickel sample is shown in Figure 40 for small potential windows and a set of cycles at a larger potential window similar to the size of the potential window for the gold-based RSMS. The redox behavior was not as defined as the gold-based RSMS, but there were still noticeable reduction and oxidation peaks. However, the current did not begin to level off near higher potentials in oxidation. The cycles with a smaller potential window would slowly decrease in current magnitude over multiple cycles, but the cycles with the greater potential window would increase over the cycles. Compared to the initial cycles with a smaller potential window, the smaller potential window cycles after large potential window cycles started out at much greater current magnitudes and stayed at those magnitudes. The areal

charge density of the nickel-based sample was 0.35 C/cm^2 and the filling efficiency for the large potential window was 31.9%. The areal charge density was very close to that of the gold-based RSMS which is desirable, as the thickness of the resulting PPy(DBS) is preferred for real-time operation of the membrane. The filling efficiency was slightly lower.

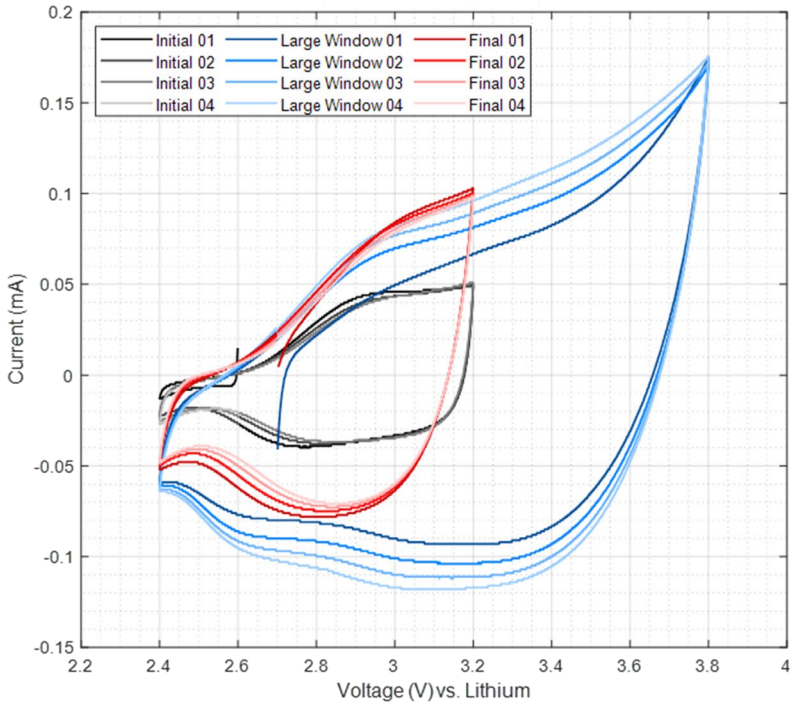

Figure 40: Cyclic voltammetry of PPy(DBS) electropolymerized on nickel sample.

The redox behavior shown by the cyclic voltammetry of PPy(DBS) on nickel/titanium and aluminum/titanium samples in Figure 41 and Figure 42 respectively behaved similarly to the PPy(DBS) on nickel sample. However, these samples greatly differed from PPy(DBS) on nickel in their areal charge densities and filling efficiencies. The PPy(DBS) on nickel/titanium areal charge density was 1.27C/cm^2 and the filling efficiency was 6.8%. The PPy(DBS) on aluminum/titanium areal charge density was 1.31C/cm^2 and the filling efficiency was 8.6%. The areal charge densities required for a full, even layer of PPy(DBS) were much higher than the

nickel-based sample. The filling efficiencies were also very low in part due to the thicker layers of PPy(DBS) having more available sites, but the additional thickness prevented as many ions from reaching those sites. A summary of the electropolymerization trials as well as the resistance of each metal substrate is shown in Table 3 on the next page.

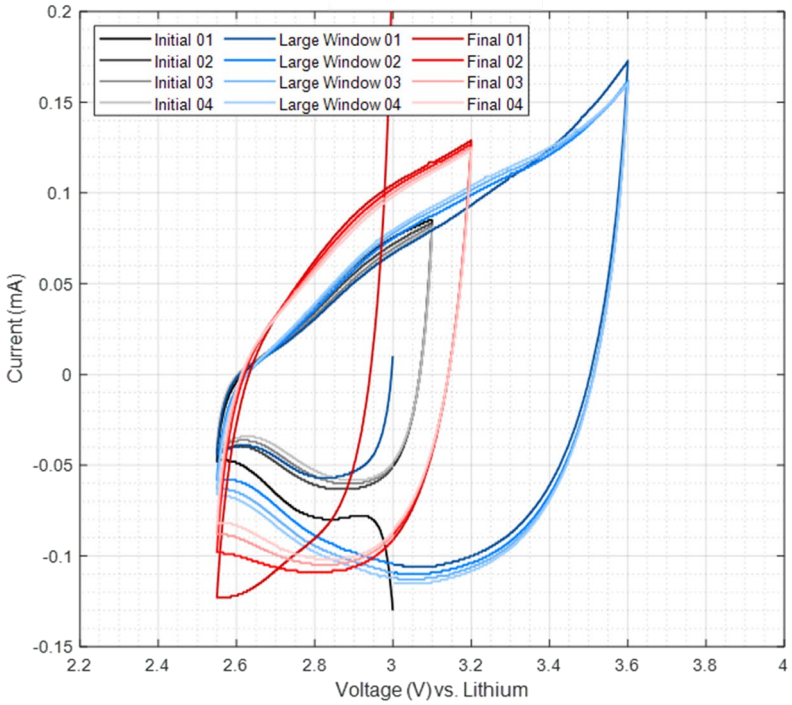

Figure 41: Cyclic voltammetry of PPy(DBS) electropolymerized on nickel/titanium sample.

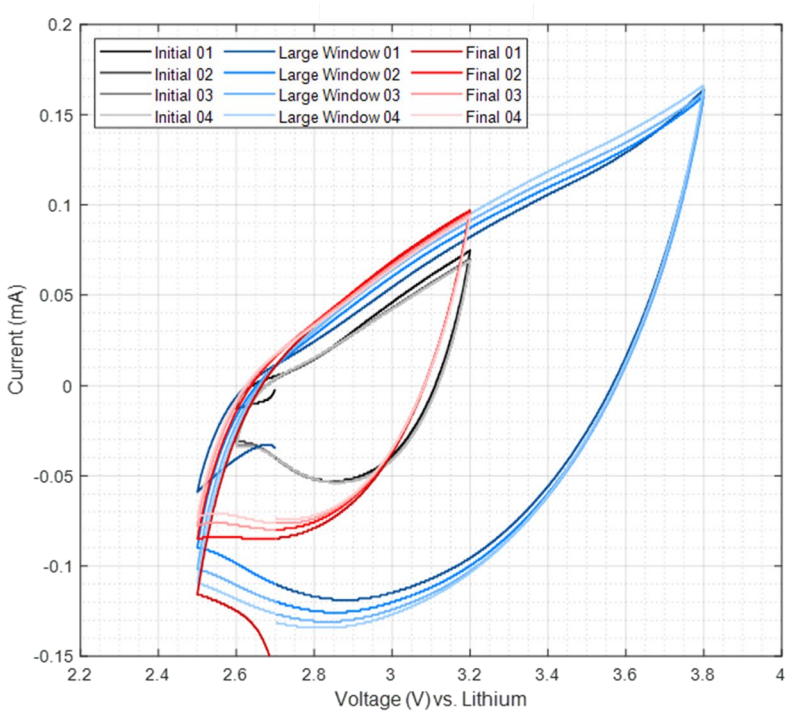

Figure 42: Cyclic voltammetry of PPy(DBS) electropolymerized on aluminum/titanium sample.

Table 3: Summary of electropolymerization trials.

Sputtered Metal	**Resistance (Ω)**	**Successful Electropolymerization Parameters**	**Areal Charge Density (C/cm^2)**	**Filling Efficiency Achieved (%)**
Au	4	0.2M pyrrole 0.1M NaDBS 0.5V	0.3	42.0
Al	12	N/A	N/A	N/A
Al/Ti	52	0.4M pyrrole 0.1M NaDBS 0.75V	1.31	8.6
Ni	13	0.2M pyrrole 0.1M NaDBS 0.5V	0.35	31.9
Ni/Ti	30	0.2M pyrrole 0.1M NaDBS 0.75V	1.27	6.8

3.4: Conclusions

In this chapter, the optimal melt tape parameters to provide effective sealing without damaging the RSMS were determined. The charge-discharge cycling performance of the pouch cell with a gold-based RSMS was shown to be comparable to the baseline pouch cells. Real-time testing of the pouch cell with a gold-based RSMS demonstrated the capability for the RSMS to reversibly shut down charging of the cell for 30 to 60 seconds or provide a power boost during discharging for approximately 60 seconds. Nickel was shown to be a potential candidate for replacing gold in the fabrication of the RSMS based on a filling efficiency of 31.9% for PPy(DBS) on nickel compared to 42.0% for PPy(DBS) on gold.

Chapter 4: Conclusion

4.1: Contributions

The purpose of this research was to develop a fabrication method for lithium-ion pouch cells with a third active electrode, a reversible shutdown membrane separator (RSMS), and characterize the performance of these pouch cells. The use of a RSMS in a lithium-ion battery architecture has been demonstrated in a Swagelok cell in previous research [11], but not in a cell configuration used in commercial applications. An additional component of this research was to explore cost effective alternatives to gold in the creation of the RSMS, as gold is not desirable for production on any appreciable scale. A novel fabrication method for pouch cells with a third active electrode, a RSMS in this case, has been developed. An important aspect of the fabrication method is the melt tape parameters necessary to provide effective sealing and a reliable current lead for control of the RSMS. Characterization of the pouch cells with a RSMS has verified the ability to counteract thermal runaway by shutting down charging of the cell for a period and to allow for higher C-rates with a period of power boost while conserving the cell capacity. This research has demonstrated nickel is a potential candidate to replace gold in a RSMS for cost reduction and presented the steps for fabricating a lithium-ion pouch cell with a nickel-based RSMS.

4.2: Future Work

This research has demonstrated the fabrication and performance of a single layer pouch cell with a gold-based RSMS. Nickel has been demonstrated to be a potential candidate for cost reduction in the fabrication of the RSMS. The functionality of a pouch cell with a gold alternative based RSMS should be demonstrated. Commercial applications would use multi-layer

pouch cells, so fabrication and characterization of multi-layer pouch cells with a RSMS must be investigated. While the single layer pouch cell fabrication method was created with the potential for roll-to-roll processing in mind, scalability of the process for mass production should be demonstrated and some adjustments may need made. The shutdown capability of cells with a RSMS must be validated under simulated thermal runaway conditions such as elevated temperature. For wider applicability, integration of a RSMS into other commercial cell architectures such as cylindrical or prismatic cells should also be explored.

The RSMS is a crucial component to these pouch cells, but thus far has been designed to build upon off the shelf battery separator material. Fabrication of the RSMS from the ground up should be studied and building a RSMS from an already conductive substrate of the right porosity could lead to greatly improved manufacturability, especially on the multi-layer and mass production scale.

References

[1] Nitta N, Wu F, Lee JT, Yushin G. “Li-ion battery materials: present and future.” *Materials Today* 2015;18(5):252-264.

[2] Maiser E. “Battery Packaging – Technology Review.” *AIP Conference Proceedings* 2014;1597:204.

[3] Wang Q, Ping P, Zhao X, Chu G, Sun J, Chen C. “Thermal runaway caused fire and explosion of lithium ion battery.” *Journal of Power Sources* 2012;208:210-224.

[4] Feng X, Ouyang M, Liu X, Lu L, Xia Y, He X. “Thermal runaway mechanism of lithium ion battery for electric vehicles: A review.” *Energy Storage Materials* 2017;10:1016.

[5] Tian R, Park S-H, King PJ, Cunningham G, Coelho J, Nicolosi V, et al. “Quantifying the factors limiting rate performance in battery electrodes.” *Nature Communications* 2019;10:1933.

[6] Winter, M. & Brodd, R. J. “What Are Batteries, Fuel Cells, and Supercapacitors?” *Chemical Reviews* 2004;104:4245–4270.

[7] Hery T, Sundaresan VB. “Ionic redox transistor from pore-spanning PPy(DBS) membranes.” *Energy Environ Sci* 2016;9:2555–62.

[8] Chen Z, Hsu P-C, Lopez J, Li Y, To JWF, Liu N, et al. “Fast and reversible thermoresponsive polymer switching materials for safer batteries.” *Nature Energy* 2016;1:15009.

[9] Baginska M, Blaiszik BJ, Merriman RJ, Sottos NR, Moore JS, White SR. “Autonomic Shutdown of Lithium-Ion Batteries Using Thermoresponsive Microspheres.” *Advanced Energy Materials* 2012;2(5):583-90.

[10] Kong L, Liu B, Ding J, Yan X, Tian G, Qi S, Wu D. “Robust polyetherimide fibrous membrane with crosslinked topographies fabricated via in-situ micro-melting and its application as superior Lithium-ion battery separator with shutdown function.” *Journal of Membrane Science* 2018;549:244-250.

[11] Hery T, Sundaresan VB. “Controlled Operation of Lithium Ion Batteries Using Reversible Shutdown Membrane Separators.” *ASME 2019 Conference on Smart Materials, Adaptive Structures, and Intelligent Systems (SMASIS2019), Louisville, KY, 9-11 September.*

[12] Wood III DL, Li J, Daniel C. “Prospects for reducing the processing cost of lithium ion batteries.” *Journal of Power Sources* 2015;275:234-242.

[13] Idla K, Inganas O, Standberg M. “Good adhesion between chemically oxidized titanium and electrochemically deposited polypyrrole.” *Electrochimica Acta* 2000;45:2121-2130.

[14] Peres RCD, De Paoli M-A, Torresi RM. “The role of ion exchange in the redox processes of polypyrrole/dodecyl sulfate films as studied by electrogravimetry using a quartz crystal microbalance.” *Synthetic Metals* 1992;48:259-270.

Appendix A

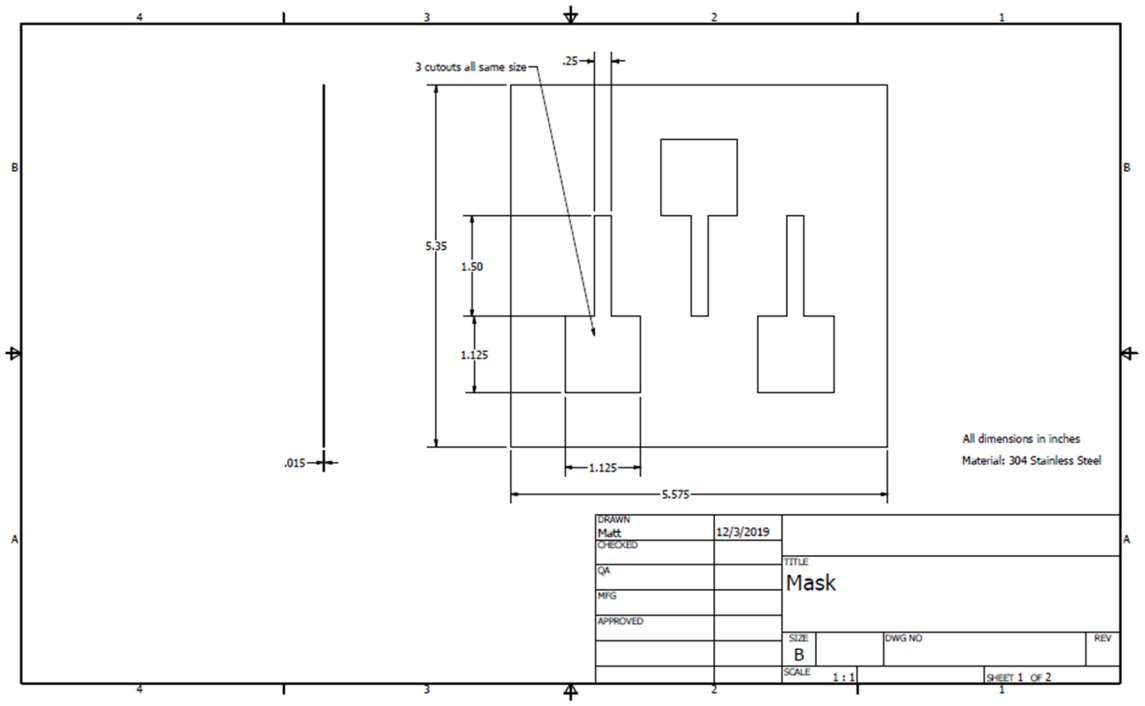

Figure A1: Drawing of mask for waterjet cutting.

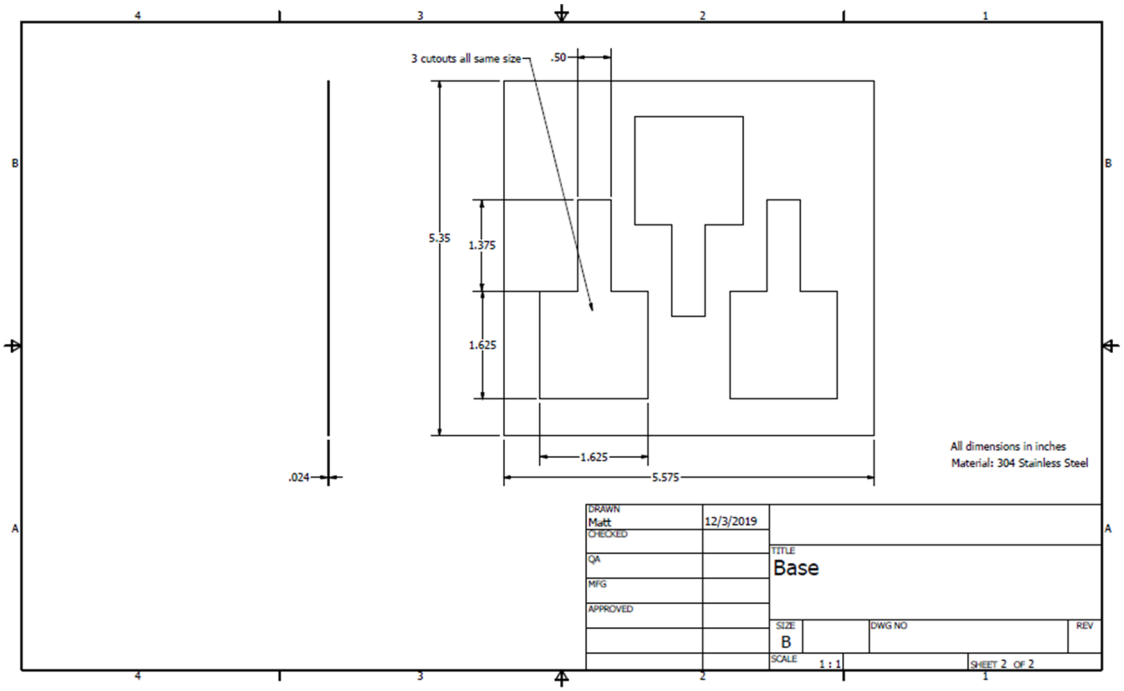

Figure A2: Drawing of die for waterjet cutting.